Optimal strategies for optical quantum memories using long-lived noble-gas spins

Or Katz [1,*,†], Eran Reches [2,3,4,*,‡], Roy Shaham [2,5,6], Eilon Poem [2], Alexey V. Gorshkov [7], and Ofer Firstenberg [2]

[1] School of Applied and Engineering Physics, Cornell University, Ithaca, New York 14853, USA
[2] Department of Physics of Complex Systems, Weizmann Institute of Science, Rehovot 76100, Israel
[3] Max-Planck-Institut für Quantenoptik, 85748 Garching, Germany
[4] Fakultät für Physik, Ludwig-Maximilians-Universität München, 80799 München, Germany
[5] Harvard-MIT Center for Ultracold Atoms, Cambridge, Massachusetts 02138, USA
[6] Department of Physics and Department of Chemistry and Chemical Biology, Harvard University, Cambridge, Massachusetts 02138, USA
[7] Joint Quantum Institute and Joint Center for Quantum Information and Computer Science, NIST/University of Maryland, College Park, Maryland 20742, USA

(Received 7 November 2024; accepted 17 November 2025; published 29 December 2025)

Nuclear spins of noble gases exhibit exceptionally long coherence times and can potentially serve as a long-lived storage medium for quantum information. We analyze and compare the performance of two mechanisms for mapping the quantum state of light onto the collective spin state of noble gases. The first mechanism utilizes collisional exchange with the electronic spin state of metastable noble-gas atoms, while the second relies on spin-exchange collisions with ground-state alkali-metal atoms. We describe the operation of an optical quantum memory relying on these two mechanisms using a compact model and study strategies that optimize the memory storage efficiency. Through numerical simulations, we identify optimal sequences for storing optical signals with different signal bandwidths and electronic spin relaxation rates. This work highlights the qualitative difference between the two approaches for using noble gases as long-lived quantum memories at noncryogenic conditions and outlines the regimes in which they are expected to be efficient.

DOI: 10.1103/xt9b-yq8q

I. INTRODUCTION

Optical quantum memories enable the storage and retrieval of nonclassical photonic signals. High-performance memories are vital for various quantum-optics applications, including quantum communication, entanglement distribution, and universal quantum computation [1–5]. The memory storage duration is ultimately limited by the coherence time of the material state utilized by the memory.

Nuclear spins in the cores of noble gases are enclosed by complete electronic shells, which isolate them from the environment [6–10]. They can maintain their quantum state for many hours and thus serve as a robust storage medium. However, their optical transparency and the absence of strong dipole transitions hinder their suitability for light-storage applications. Electronic spins in atoms, however, can act as mediators, efficiently coupling to photons via the dipole interaction and enabling access to nuclear spins through magnetic-like interaction. Nuclear spins in noble gases can couple to the electronic spins of another optically accessible atomic ensemble through random collisions. The latter ensemble can be either a noble gas in an electronically excited metastable state, where the coupling occurs via metastability-exchange collisions governed by the Coulomb interaction [11], or an alkali-metal vapor in its electronic ground state, where the Fermi-contact interaction mediates the coupling [12,13]. Both collisional mechanisms have been proposed as interfaces for utilizing noble-gas spins as long-lived optical quantum memories [11,14], primarily focusing on ultralow-bandwidth signals or configurations where the mediator's relaxation is negligible.

The memory performance depends on a set of input control fields, which shape the response of the spins and determine their efficiency to store or retrieve photons. For optically accessible memories in a standard Λ configuration, optimal control analysis reveals an optimal mapping that enables storage of finite bandwidth optical signals via temporal shaping of an optical control field [15,16], with recent extensions for high-bandwidth pulses [17] or single photon-generation schemes [18,19]. In the absence of spin relaxation, this mapping features a universal memory efficiency, which depends exclusively on the degree of optical coupling (e.g., optical depth or cooperativity). However, in quantum memories based on nuclear spins, the magnetic-like coupling strength between nuclear and electronic spins is fixed, and can be further ac-

*These authors contributed equally to this work.
†Contact author: or.katz@cornell.edu
‡Contact author: eran.reches@mpq.mpg.de

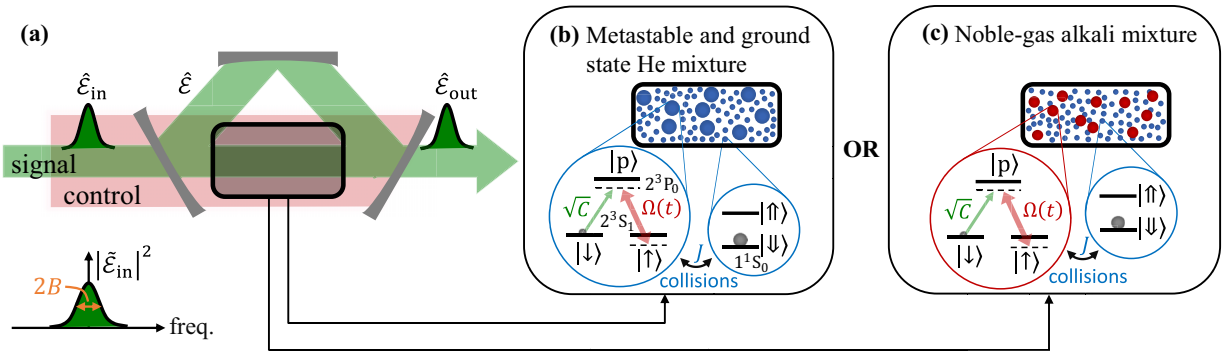

FIG. 1. Optical quantum memory using nuclear spins of noble gases. (a) An input optical signal (green) is coherently mapped, via electronic spins, onto the state of noble-gas spins. $\hat{\mathcal{E}}$ denotes the annihilation operator of the optical field in the cavity. $\hat{\mathcal{E}}_{\rm in}$ ($\hat{\mathcal{E}}_{\rm out}$) is the annihilation operator for the input (output) optical field. The input pulse has a bandwidth $2B$, where $\tilde{\mathcal{E}}_{\rm in}$ is the Fourier transform of the input pulse. Our simple model qualitatively describes platforms where the electronic spins are either (b) of noble gases in a metastable state, e.g., ^{3}He, or (c) of alkali-metal atoms in their electronic ground state. $\Omega(t)$ is the Rabi frequency of the optical control field. J is the fixed, magnetic-like coupling between the nuclear and electronic spins; it originates from metastability-exchange collisions in panel (b), and from spin-exchange collisions in panel (c).

companied by non-negligible relaxation of the electron spins. Consequently, the standard optimal storage protocols, which, e.g., rely on temporal shaping of the coupling strengths, are no longer applicable.

Here, we study the storage of light onto the collective nuclear spin of an ensemble of noble-gas atoms. We numerically analyze optimal strategies and compare the two main approaches for such a memory, which are based on either metastability-exchange or spin-exchange collisions with excited-state noble gases or alkali-metal atoms, respectively. For both approaches, we study numerically optimized solutions for variable optical bandwidth of the signal and nonzero relaxation of the mediator, extending previous analyses. We observe that the metastability-exchange approach demonstrates highly efficient storage only for low-bandwidth signals, where the signal is protected via mapping onto a decoherence-free subspace, whereas at higher bandwidths, optimal pulses can achieve moderate efficiencies via nonadiabatic solutions. For the case of spin-exchange collisions, our analysis extends previous analytical protocols and shows that efficient memory operation can be realized for a large range of bandwidths and magneticlike coupling strengths. Our study delineates the necessary conditions for implementing efficient, hours-long quantum memories under noncryogenic conditions.

The paper is organized as follows: In Sec. II, we present the model studied in this work, consisting of an ensemble of noble-gas spins coupled via collisions to an ensemble of electron spins, which in turn interact with a single mode of an optical cavity. We provide the full equations of motion, describe the adiabatic elimination of the optical coherence, and define the storage efficiency as a key metric for evaluating memory performance. In Sec. III, we look in detail into the structure of this efficiency and reveal it's general form, mapping the relevant parameters. In Sec. IV, we study analytically storage of light based on metastability-exchange collisions with an electronically excited noble gas. In Sec. V, we present the main analytical results of Ref. [14] for storage of light based on spin-exchange collisions with alkali-metal vapor. In Sec. VI, we extend these analyses through numerical optimization of the storage sequences for both memory configurations and compare their performance. We discuss the implications of these results in Sec. VII.

II. MODEL

In this section, we present the model studied in this work: an ensemble of noble-gas spins coupled through collisions to an ensemble of electron spins, which in turn interacts with a single optical cavity mode.

A. Equations of motion

The system we consider, illustrated in Fig. 1, consists of nuclear spins of noble gases and an ensemble of electronic spins. In Fig. 1(b), the electronic spins correspond to metastable noble-gas atoms, while in Fig. 1(c), they represent alkali-metal atoms. The electronic spins interact with an optical signal field $\hat{\mathcal{E}}$ through the electric-dipole interaction. Each electron spin is modeled as a Λ-system with two spin levels ($|\downarrow\rangle$ and $|\uparrow\rangle$) in the electronic ground state and one electronically excited state $|p\rangle$, an approximation valid when the excitation bandwidth and the generalized Rabi frequency (including detuning) are both much smaller than the excited-state energy-level separation, and also under certain conditions in the far-off-resonant regime as discussed in Sec. VII. To simplify the model, we work with a single-mode cavity described by the annihilation operator $\hat{\mathcal{E}}$ and coupled to the symmetric, collective, and optical dipole described by annihilation operator $\hat{\mathcal{P}} \equiv \frac{1}{\sqrt{N_{\rm a}}}\sum_a |\downarrow\rangle_a\langle {\rm p}|_a$ (i.e., driving the $|\downarrow\rangle - |{\rm p}\rangle$ transition), where $N_{\rm a} \gg 1$ is the number of electronic spins. A classical control field with Rabi frequency $\Omega(t)$ drives the $|{\rm p}\rangle - |\uparrow\rangle$ transition, thereby coupling the signal field to the collective electron spin coherence with the annihilation operator $\hat{\mathcal{S}} \equiv \frac{1}{\sqrt{N_{\rm a}}}\sum_a |\downarrow\rangle_a\langle\uparrow|_a$ [16]. This two-photon process circumvents the rapid decoherence of the optical dipole $\hat{\mathcal{P}}$ (e.g., due to spontaneous emission, pressure broadening, or inhomogeneous broadening) and, by modulation of $\Omega(t)$, allows for the storage of the optical signal on and its retrieval from the

spin $\hat{\mathcal{S}}$. At this point, $\hat{\mathcal{S}}$ may serve as a quantum memory for $N \ll N_a$ photons, whose lifetime is limited by the relaxation rate γ_s of the electron spins [20–26].

We consider N_b spin-1/2 nuclei with down and up spin states $|\Downarrow\rangle$, $|\Uparrow\rangle$, as shown in Figs. 1(b) and 1(c). These spins, which we use as our quantum memory, weakly interact with their surroundings. As a result, their collective spin annihilation operator $\hat{\mathcal{K}} \equiv \frac{1}{\sqrt{N_b}} \sum_b |\Downarrow\rangle_b\langle\Uparrow|_b$ has extremely low decoherence rate $\gamma_k \ll \gamma_s$ [13].

When the optical input signal with temporal bandwidth $2B$ enters the cavity, it interacts with the optical dipole and, in the fast-cavity limit, gives rise to the output field [16]

$$\hat{\mathcal{E}}_{\text{out}} = \hat{\mathcal{E}}_{\text{in}} + i\sqrt{2\gamma_p C}\hat{\mathcal{P}}. \tag{1}$$

C is the cooperativity, which characterizes the atom-photon interaction strength and is proportional to the product of the cavity finesse and the optical depth of the atomic medium [27,28]. γ_p denotes the dephasing rate of the atomic optical dipole and $\gamma_p C$ corresponds to its stimulated emission rate [14].

The two systems differ in terms of the nature of the electronic spins and the coupling mechanism between the electronic and nuclear spins. However, for spin-polarized ensembles, we can describe the dynamics of both approaches using the Bloch-Heisenberg-Langevin model in a concise manner [29,30]. While the complete equations, which include quantum noise terms, are stochastic, the memory efficiency and bandwidth are governed by the deterministic part, which is described by[1]

$$\partial_t\hat{\mathcal{P}} = -(\gamma_p(C+1) + i\Delta)\hat{\mathcal{P}} + i\Omega\hat{\mathcal{S}} + i\sqrt{2\gamma_p C}\hat{\mathcal{E}}_{\text{in}}, \tag{2}$$

$$\partial_t\hat{\mathcal{S}} = -(\gamma_s + i\delta_s)\hat{\mathcal{S}} + i\Omega^*\hat{\mathcal{P}} - iJ\hat{\mathcal{K}}, \tag{3}$$

$$\partial_t\hat{\mathcal{K}} = -(\gamma_k + i\delta_k)\hat{\mathcal{K}} - i\xi J\hat{\mathcal{S}}. \tag{4}$$

Here, Δ denotes the (single-photon) detuning of the atomic optical transition from the cavity resonance, δ_s is the Raman (two-photon) detuning, and δ_k is the detuning of the entire three-step process. J denotes the collective magneticlike coupling rate between the electronic and nuclear spin ensembles. The parameter $\xi = \mp 1$ differentiates between the two experimental configurations we study: $\xi = -1$ describes metastability-exchange dynamics for collisions with noble-gas atoms in a metastable state (see Appendix A for derivation based on Ref. [11]), whereas $\xi = +1$ describes the spin-exchange dynamics for collisions with alkali-metal atoms, as derived in Ref. [13].

We aim to find and characterize a controllable and reversible process that efficiently transfers the quantum excitations from $\hat{\mathcal{E}}_{\text{in}}$ to the nuclear spins $\hat{\mathcal{K}}$ and then back from $\hat{\mathcal{K}}$ to $\hat{\mathcal{E}}_{\text{out}}$. In the following, it is important to note that the parameter γ_s is not negligible, and the coupling J between $\hat{\mathcal{S}}$ and $\hat{\mathcal{K}}$ remains constant, which limits the applicability of the temporal control typically utilized in Λ-type memories [16].

[1]The stochastic part is mainly responsible for the preservation of commutation relations through the introduction of vacuum noise [5,13,16]. Specific noise terms for this model are provided in Refs. [14,31].

B. Adiabatic elimination of the optical coherence

In this work, we focus on the regime where $|\gamma_p C + i\Delta| \gg B, |\Omega|, |\partial_t\Omega/\Omega|, J$, ensuring that the dynamics of the electronically excited level $|p\rangle$, and therefore the optical dipole $\hat{\mathcal{P}}$, are much faster than the ground-state coherences associated with $\hat{\mathcal{S}}$ and $\hat{\mathcal{K}}$ [11,14,16]. In this regime,[2] the optical dipole operator in Eq. (3) is in a quasisteady state, approximately satisfying $\partial_t\hat{\mathcal{P}} = 0$ in Eq. (2). This leads to

$$\hat{\mathcal{P}} = \frac{i\Omega\hat{\mathcal{S}} + i\sqrt{2\gamma_p C}\hat{\mathcal{E}}_{\text{in}}}{\gamma_p(C+1) + i\Delta}, \tag{5}$$

which, when substituted into Eq. (3), yields the simplified dynamics of the alkali-metal spins:

$$\partial_t\hat{\mathcal{S}} = -(\gamma_s + \Gamma_\Omega + i\delta_s)\hat{\mathcal{S}} - iJ\hat{\mathcal{K}} - Q\Omega^*\hat{\mathcal{E}}_{\text{in}}. \tag{6}$$

Note that the excitation $\langle\hat{\mathcal{P}}^\dagger\hat{\mathcal{P}}\rangle \ll 1$ remains small in this regime, further ensuring that $\hat{\mathcal{P}}$ adiabatically follows the ground-state spin coherence and the slowly varying input field. Following Ref. [14], we define the quantities

$$\Gamma_\Omega \equiv \frac{|\Omega|^2}{\gamma_p(C+1) + i\Delta}, \tag{7}$$

$$Q \equiv \frac{\sqrt{2\gamma_p C}}{\gamma_p(C+1) + i\Delta}. \tag{8}$$

Intuitively, Γ_Ω represents the rate at which photons are retrieved via the alkali-metal spins during retrieval, while $Q\Omega^*$ characterizes the rate at which the input field couples to the alkali-metal spins during storage. Equations (4) and (6) thus describe the evolution of ground-state spin coherence during both storage and retrieval.

C. Storage efficiency

To characterize memory performance, we focus on storage efficiency as the primary metric. It is defined as the ratio of collective spin excitations stored in the long-lived collective spin mode to the number of input optical excitations (signal photons) [16]. The storage efficiency is given by [14]

$$\eta = \frac{\langle\hat{\mathcal{K}}_\alpha^\dagger(T_f)\hat{\mathcal{K}}_\alpha(T_f)\rangle}{\int_{-\infty}^{T_f}\langle\mathcal{E}_{\text{in}}^\dagger(t)\mathcal{E}_{\text{in}}(t)\rangle dt}, \tag{9}$$

where T_f denotes the time at which the storage process between photons and spins is complete. The operator $\hat{\mathcal{K}}_\alpha = \alpha_K\hat{\mathcal{K}} + \alpha_S\hat{\mathcal{S}}$ represents a bosonic annihilation operator[3] associated with the longest-lived collective spin coherence of the electronic and noble-gas spins, satisfying $[\hat{\mathcal{K}}_\alpha, \hat{\mathcal{K}}_\alpha^\dagger] = 1$. As discussed below, for spin-exchange collisions with alkali-metal atoms, we have $\alpha_S = 0$ and $\alpha_K = 1$, so that $\hat{\mathcal{K}}_\alpha = \hat{\mathcal{K}}$. For metastable-exchange collisions, we have $\alpha_S \ll \alpha_K$, meaning that in both cases, $\hat{\mathcal{K}}_\alpha$ is either entirely or nearly a collective noble-gas spin excitation.

[2]Gorshkov, *et al.* [16] demonstrate that for three-level systems, the condition $|\gamma_p C + i\Delta| \gg B$ is sufficient to ensure adiabatic following under optimal storage and retrieval.

[3]The collective spin operators for large atomic ensembles are treated as bosonic operators within the Holstein-Primakoff approximation (see, e.g., [5,13]).

III. MATHEMATICAL STRUCTURE OF THE STORAGE EFFICIENCY

In this section, we analyze the mathematical structure of the storage efficiency and identify its dependencies on system parameters.

Equations (1)–(4) are linear in the spin and photonic operators, meaning that the results for storage efficiency are independent of the number of photons in the signal (N). Therefore, for all efficiency calculations, we set $N = \int_{-\infty}^{T'} |\mathcal{E}_{\rm in}(t)|^2 dt = 1$ corresponding to a single incoming photon. This simplifies the efficiency expression in Eq. (9) to $\eta = \langle \hat{\mathcal{K}}_\alpha^\dagger(T')\hat{\mathcal{K}}_\alpha(T')\rangle$. However, we emphasize that these memories are not limited to single-photon storage and can, in principle, store any distribution of photonic excitations associated with the input field.

To identify how the storage efficiency depends on system parameters, we rewrite the equations of motion in normalized units. We start by defining $\gamma_\Omega \equiv \mathrm{Re}(\Gamma_\Omega)$ and $\delta_\Omega \equiv \mathrm{Im}(\Gamma_\Omega)$ as the real and imaginary parts of the power broadening rate Γ_Ω from Eq. (7). We then rewrite the term

$$Q\Omega^* = \sqrt{\frac{\Gamma_\Omega}{\Gamma_\Omega^*}}\sqrt{\frac{\Omega^*}{\Omega}}\sqrt{2\gamma_\Omega}\sqrt{\frac{C}{C+1}} \tag{10}$$

in Eq. (6) [see also Eq. (8)], noting that the first two factors are complex numbers with unit modulus. We define the phase notation $e^{i\phi_\Omega} = \sqrt{\Gamma_\Omega/\Gamma_\Omega^*}\sqrt{\Omega^*/\Omega}$ and rewrite Eq. (6) as

$$\begin{aligned}\partial_t \hat{\mathcal{S}} = &-(\gamma_{\rm s} + \gamma_\Omega + i(\delta_{\rm s} + \delta_\Omega))\hat{\mathcal{S}} - iJ\hat{\mathcal{K}} \\ &- e^{i\phi_\Omega}\sqrt{2\gamma_\Omega}\sqrt{\tfrac{C}{C+1}}\hat{\mathcal{E}}_{\rm in}.\end{aligned} \tag{11}$$

To eliminate the phase factor, we apply the transformation $\hat{\mathcal{S}} \to e^{i\phi_\Omega}\hat{\mathcal{S}}$ and $\hat{\mathcal{K}} \to e^{i\phi_\Omega}\hat{\mathcal{K}}$, which does not affect the storage efficiency in Eq. (9). This transformation modifies Eqs. (4) and (11) into

$$\partial_t \hat{\mathcal{S}} = -(\gamma_{\rm s} + \gamma_\Omega + i\bar{\delta}_{\rm s})\hat{\mathcal{S}} - iJ\hat{\mathcal{K}} - \sqrt{2\gamma_\Omega}\sqrt{\eta_C}\hat{\mathcal{E}}_{\rm in}, \tag{12}$$

$$\partial_t \hat{\mathcal{K}} = -(\gamma_{\rm k} + i\bar{\delta}_{\rm k})\hat{\mathcal{K}} - i\xi J\hat{\mathcal{S}}, \tag{13}$$

where the detunings are shifted as $\bar{\delta}_{\rm s} = \delta_{\rm s} + \delta_\Omega + \partial_t\phi_\Omega$ and $\bar{\delta}_{\rm k} = \delta_{\rm k} + \partial_t\phi_\Omega$, and the partial efficiency

$$\eta_C = \frac{C}{C+1} \tag{14}$$

denotes the maximal storage efficiency in three-level systems, determined by the cooperativity C [16]. Finally, we introduce dimensionless variables by defining the dimensionless time $\tau = \gamma_{\rm s}t$, leading to

$$\partial_\tau \hat{\mathcal{S}} = -\left(1 + \tfrac{\gamma_\Omega}{\gamma_{\rm s}} + \tfrac{i\bar{\delta}_{\rm s}}{\gamma_{\rm s}}\right)\hat{\mathcal{S}} - \tfrac{iJ}{\gamma_{\rm s}}\hat{\mathcal{K}} - \sqrt{\tfrac{2\gamma_\Omega}{\gamma_{\rm s}}}\hat{\mathcal{E}}'_{\rm in}, \tag{15}$$

$$\partial_\tau \hat{\mathcal{K}} = -\left(\tfrac{\gamma_{\rm k}}{\gamma_{\rm s}} + \tfrac{i\bar{\delta}_{\rm k}}{\gamma_{\rm s}}\right)\hat{\mathcal{K}} - i\xi\tfrac{J}{\gamma_{\rm s}}\hat{\mathcal{S}}. \tag{16}$$

The normalized field $\hat{\mathcal{E}}'_{\rm in}(\tau) = \sqrt{\eta_C}\hat{\mathcal{E}}_{\rm in}(\tau)/\sqrt{\gamma_{\rm s}}$ now contains $\eta_C = C/(C+1)$ excitations, depending only on the cavity cooperativity with the electron-spin ensemble, and has a dimensionless bandwidth $2B/\gamma_{\rm s}$. From Eqs. (15)–(16), we deduce that the storage efficiency takes the form

$$\eta(C, \gamma_{\rm k}, \gamma_{\rm s}, J, B) = \eta_C\eta_\infty\left(\frac{\gamma_{\rm k}}{\gamma_{\rm s}}, \frac{J}{\gamma_{\rm s}}, \frac{B}{\gamma_{\rm s}}, \xi\right), \tag{17}$$

with control fields $\gamma_\Omega(t)/\gamma_{\rm s}$, $\bar{\delta}_{\rm s}(t)/\gamma_{\rm s}$, and $\bar{\delta}_{\rm k}(t)/\gamma_{\rm s}$ that can be optimized to maximize efficiency.

As a consistency check, we numerically examined the dependence of the storage efficiency on C for the adiabatic and sequential strategies in Secs. V B and V C. These results, presented in Appendix B, show excellent agreement with Eq. (17).

IV. MEMORIES BASED ON METASTABILITY-EXCHANGE COLLISIONS

In this section, we analytically study the storage of light based on metastability-exchange collisions with an electronically excited noble gas. We identify the decoherence-free subspace associated with the metastability-exchange coupling that is suitable for the memory operation and estimate the storage efficiency in the adiabatic regime.

A. Physical mechanism

The nuclear spin of noble-gas atoms in the electronic ground state can be coupled with the spins of atoms in a metastable electronically excited state through collisions. The ensemble of metastable atoms is typically generated and maintained using pulses of electrical discharge. While the study of various noble-gas atoms has been conducted [32,33], in this work, we focus on an ensemble of ^{3}He atoms, which is commonly considered in practical applications [7,10,34]. We refer to the electronic ground-state manifold as 1^1S_0 and the electronic metastable manifold as 2^3S_1. The excited electronic manifold is 2^3P_0. The excited- and metastable-state manifolds can be controlled through optical transitions at 1083 nm, whereas the ground- and metastable-state manifolds exchange electronic configurations due to the exchange interaction in the so-called metastability- exchange collisions.

We adopt the assumptions presented in Ref. [11], which analyzed storage and retrieval of squeezed light, and assume that the dominant relaxation mechanism for helium atoms is the metastability-exchange process, neglecting all other relaxation mechanisms. Under these assumptions, the relaxation rates are given by $\gamma_{\rm s}$ for the metastable population and $\gamma_{\rm k} = r\gamma_{\rm s}$ for the ground-state population, where r denotes the fraction of helium atoms in the metastable state relative to the ground-state population. The magnetic-like coupling rate is given by $J = \sqrt{\gamma_{\rm k}\gamma_{\rm s}} = \gamma_{\rm s}\sqrt{r}$. While these equations remain valid for any ratio of metastable to ground-state noble-gas atoms ($r \geqslant 0$), in practical applications [7], the fraction of helium atoms in the metastable state is typically much smaller than the ground-state population, such that $r \ll 1$. Consequently, the relations $\gamma_{\rm k} \ll J \ll \gamma_{\rm s}$ are ensured and directly determined by the small fraction of metastable-state atoms.

These assumptions are consistent with experimentally achievable parameters. At low helium pressures, the metastability-exchange collision rate for the metastable state $\gamma_{\rm s}$ is proportional to the gas pressure, with a coefficient of $3.8 \times 10^6\ \mathrm{s}^{-1}/\mathrm{mbar}$, while the metastable-state fraction is

approximately $r \approx 10^{-6}$ [35]. Excited-state collisions involving the $|p\rangle$ level occur at rates on the order of a few $10^7\ \mathrm{s}^{-1}/\mathrm{mbar}$ [36,37]. Other relaxation mechanisms affecting the metastable state, such as atomic de-excitation followed by re-excitation in the plasma or through wall collisions, typically occur at rates of approximately $10^3\ \mathrm{s}^{-1}$ [7,34]. Thus, for helium pressures on the order of 1 mbar or higher, these additional relaxation mechanisms are negligible compared to the metastability-exchange rate.

B. Coupled-spin dynamics in the dark

To highlight the memory mechanism, particularly the emergence of a decoherence-free subspace, we first examine the interplay between $\hat{\mathcal{S}}$ and $\hat{\mathcal{K}}$ in the absence of external fields ($\Omega = 0$ and $\langle \hat{\mathcal{E}}_{\mathrm{in}}^\dagger \hat{\mathcal{E}}_{\mathrm{in}} \rangle = 0$). We also assume on-resonance operation, setting $\bar{\delta}_{\mathrm{s}} = \bar{\delta}_{\mathrm{k}} = 0$. Taking $\xi = -1$ and substituting into Eqs. (12) and (13) yields the coupled-spin dynamics

$$\partial_t \begin{pmatrix} \hat{\mathcal{S}} \\ \hat{\mathcal{K}} \end{pmatrix} = \begin{pmatrix} -\gamma_{\mathrm{s}} & -i\sqrt{\gamma_{\mathrm{s}}\gamma_{\mathrm{k}}} \\ i\sqrt{\gamma_{\mathrm{s}}\gamma_{\mathrm{k}}} & -\gamma_{\mathrm{k}} \end{pmatrix} \begin{pmatrix} \hat{\mathcal{S}} \\ \hat{\mathcal{K}} \end{pmatrix}. \tag{18}$$

We now define the operators

$$\hat{\mathcal{S}}_r = (\hat{\mathcal{S}} + i\sqrt{r}\hat{\mathcal{K}})/\sqrt{1+r}, \tag{19}$$

$$\hat{\mathcal{K}}_r = (\hat{\mathcal{K}} + i\sqrt{r}\hat{\mathcal{S}})/\sqrt{1+r}, \tag{20}$$

dressed by the metastability-exchange interaction, which form an alternative set of bosonic operators and are eigenmodes of the matrix in Eq. (18). These operators satisfy $[\hat{\mathcal{S}}_r, \hat{\mathcal{S}}_r^\dagger] = [\hat{\mathcal{K}}_r, \hat{\mathcal{K}}_r^\dagger] = 1$ and $[\hat{\mathcal{S}}_r, \hat{\mathcal{K}}_r] = [\hat{\mathcal{S}}_r, \hat{\mathcal{K}}_r^\dagger] = 0$ and preserve the total number of excitations $\hat{\mathcal{S}}_r^\dagger \hat{\mathcal{S}}_r + \hat{\mathcal{K}}_r^\dagger \hat{\mathcal{K}}_r = \hat{\mathcal{S}}^\dagger \hat{\mathcal{S}} + \hat{\mathcal{K}}^\dagger \hat{\mathcal{K}}$, but, through Eq. (18), decay at different rates

$$\partial_t \begin{pmatrix} \hat{\mathcal{S}}_r \\ \hat{\mathcal{K}}_r \end{pmatrix} = -\begin{pmatrix} \gamma_{\mathrm{s}} + \gamma_{\mathrm{k}} & 0 \\ 0 & 0 \end{pmatrix} \begin{pmatrix} \hat{\mathcal{S}}_r \\ \hat{\mathcal{K}}_r \end{pmatrix}, \tag{21}$$

such that $\hat{\mathcal{S}}_r$ relaxes quickly at a rate $\gamma_{\mathrm{s}} + \gamma_{\mathrm{k}} = (1+r)\gamma_{\mathrm{s}}$, while $\hat{\mathcal{K}}_r$ does not decay. Therefore, the Fock space spanned by $\hat{\mathcal{K}}_r$ can be considered as a decoherence-free subspace suitable for a long-lived quantum memory.

C. Memory dynamics

Using the dressed operators, we can express Eqs. (12) and (13) in the presence of light as

$$\begin{aligned} \partial_t \hat{\mathcal{S}}_r = &-[\gamma_{\mathrm{s}}(1+r) + \tilde{\gamma}_\Omega + i\tilde{\delta}_{\mathrm{s}} + ir\tilde{\delta}_{\mathrm{k}}]\hat{\mathcal{S}}_r \\ &+ \sqrt{r}(\tilde{\delta}_{\mathrm{k}} - \tilde{\delta}_{\mathrm{s}} + i\tilde{\gamma}_\Omega)\hat{\mathcal{K}}_r - \sqrt{2\tilde{\gamma}_\Omega}\sqrt{\eta_C}\hat{\mathcal{E}}_{\mathrm{in}}, \end{aligned} \tag{22}$$

$$\begin{aligned} \partial_t \hat{\mathcal{K}}_r = &-(r\tilde{\gamma}_\Omega + i\tilde{\delta}_{\mathrm{k}} + ir\tilde{\delta}_{\mathrm{s}})\hat{\mathcal{K}}_r - \sqrt{r}(\tilde{\delta}_{\mathrm{k}} - \tilde{\delta}_{\mathrm{s}} + i\tilde{\gamma}_\Omega)\hat{\mathcal{S}}_r \\ &- i\sqrt{r}\sqrt{2\tilde{\gamma}_\Omega}\sqrt{\eta_C}\hat{\mathcal{E}}_{\mathrm{in}}, \end{aligned} \tag{23}$$

where again $\gamma_\Omega = \mathrm{Re}(\Gamma_\Omega)$ represents the power broadening of the optical line by the control field. All variables with a tilde are rescaled by $(1+r)$, i.e., $\tilde{\gamma}_\Omega \equiv \gamma_\Omega/(1+r)$, $\tilde{\delta}_{\mathrm{s}} \equiv \bar{\delta}_{\mathrm{s}}/(1+r)$ and $\tilde{\delta}_{\mathrm{k}} \equiv \bar{\delta}_{\mathrm{k}}/(1+r)$.

In the presence of light, collective spin excitations of alkali-metal or noble-gas spins can be coherently exchanged with photons of the input and output signal fields, while the total number of excitations decays through atomic relaxation. Following a derivation similar to Ref. [14], [4] we find that the loss of excitations is governed by

$$\begin{aligned} &\partial_t(\langle \hat{\mathcal{P}}^\dagger \hat{\mathcal{P}} \rangle + \langle \hat{\mathcal{S}}_r^\dagger \hat{\mathcal{S}}_r \rangle + \langle \hat{\mathcal{K}}_r^\dagger \hat{\mathcal{K}}_r \rangle) + \langle \hat{\mathcal{E}}_{\mathrm{out}}^\dagger \hat{\mathcal{E}}_{\mathrm{out}} \rangle - \langle \hat{\mathcal{E}}_{\mathrm{in}}^\dagger \hat{\mathcal{E}}_{\mathrm{in}} \rangle \\ &\quad = -2\gamma_{\mathrm{p}} \langle \hat{\mathcal{P}}^\dagger \hat{\mathcal{P}} \rangle - 2(\gamma_{\mathrm{s}} + \gamma_{\mathrm{k}}) \langle \hat{\mathcal{S}}_r^\dagger \hat{\mathcal{S}}_r \rangle, \end{aligned} \tag{24}$$

demonstrating that memory relaxation can be mitigated by maintaining $\langle \hat{\mathcal{P}}^\dagger \hat{\mathcal{P}} \rangle, \langle \hat{\mathcal{S}}_r^\dagger \hat{\mathcal{S}}_r \rangle \ll 1$ small during the memory operation.

D. Adiabatic mapping

The above analysis motivates consideration of a direct adiabatic mapping between $\hat{\mathcal{E}}_{\mathrm{in}}$ and $\hat{\mathcal{K}}_r$ for storage, and between $\hat{\mathcal{K}}_r$ and $\hat{\mathcal{E}}_{\mathrm{out}}$ for retrieval, maintaining $\langle \hat{\mathcal{P}}^\dagger \hat{\mathcal{P}} \rangle \ll 1$ and $\langle \hat{\mathcal{S}}_r^\dagger \hat{\mathcal{S}}_r \rangle \ll 1$ for high memory efficiency. We can construct such a mapping by considering the regime in which the electronic spin dynamics is much faster than that of the noble-gas nuclear spin, where we focus on the limit $\gamma_\Omega \gg B, \gamma_{\mathrm{s}}$. Under these conditions, $\hat{\mathcal{S}}_r$ reaches a quasisteady state and adiabatically follows the external fields. This is derived by setting $\partial_t \hat{\mathcal{S}}_r = 0$ in Eq. (22), which yields

$$\hat{\mathcal{S}}_r = \frac{1}{\gamma_{\mathrm{s}}(1+r) + \tilde{\gamma}_\Omega}(i\sqrt{r}\tilde{\gamma}_\Omega \hat{\mathcal{K}}_r - \sqrt{2\eta_C \tilde{\gamma}_\Omega}\hat{\mathcal{E}}_{\mathrm{in}}). \tag{25}$$

Here, for simplicity, we set the detunings to zero: $\tilde{\delta}_{\mathrm{s}} = \tilde{\delta}_{\mathrm{k}} = 0$.

For these conditions and the slowly varying input field, the excitation of the electron spin is small $\langle \hat{\mathcal{S}}_r^\dagger \hat{\mathcal{S}}_r \rangle \ll 1$. Substituting the expression for $\hat{\mathcal{S}}_r$ into Eq. (23), we obtain the dynamics of the collective nuclear spins during the memory operation:

$$\partial_t \hat{\mathcal{K}}_r = -\frac{r(1+r)\gamma_{\mathrm{s}}\tilde{\gamma}_\Omega}{\gamma_{\mathrm{s}}(1+r) + \tilde{\gamma}_\Omega}\left(\hat{\mathcal{K}}_r + i\sqrt{\frac{2C}{r\tilde{\gamma}_\Omega(C+1)}}\hat{\mathcal{E}}_{\mathrm{in}}\right). \tag{26}$$

To solve Eq. (26), we note that the solution for a general linear equation of the form

$$\partial_t \hat{\mathcal{K}}_r = -\mu \hat{\mathcal{K}}_r + \chi \hat{\mathcal{E}}_{\mathrm{in}} \tag{27}$$

is given by

$$\hat{\mathcal{K}}_r(0) - \hat{\mathcal{K}}_r(-\infty) = \int_{-\infty}^{0} \chi(t) e^{-\int_t^0 \mu(s)\mathrm{d}s} \hat{\mathcal{E}}_{\mathrm{in}}(t)\mathrm{d}t. \tag{28}$$

Equation (28) establishes a mapping between $\hat{\mathcal{E}}_{\mathrm{in}}$ and $\hat{\mathcal{K}}_r$ during the storage of the incoming signal. Absent any initial spin excitations, we can assume $\langle \hat{\mathcal{K}}_r^\dagger(-\infty)\hat{\mathcal{K}}_r(-\infty)\rangle = 0$. Comparison of Eq. (26) to Eq. (27) shows that μ and χ depend on γ_Ω, whose time-dependent profile can be shaped to achieve different mappings that could maximize storage efficiency.

To provide intuition for this solution, we consider first a specific example where the input signal has an exponentially shaped profile with bandwidth $2B$. Following similar derivations in Refs. [14,16], after substituting Eq. (28) into Eq. (9), we find that the storage efficiency is maximized for a time-independent control profile with amplitude

$$\tilde{\gamma}_\Omega = \frac{B\gamma_{\mathrm{s}}(1+r)}{\gamma_{\mathrm{s}} r(1+r) - B}. \tag{29}$$

[4] That is, assuming $\partial_t \langle \hat{\mathcal{O}}^\dagger \hat{\mathcal{O}} \rangle = \langle (\partial_t \hat{\mathcal{O}}^\dagger)\hat{\mathcal{O}} \rangle + \langle \hat{\mathcal{O}}^\dagger \partial_t \hat{\mathcal{O}} \rangle$ for $\hat{\mathcal{O}} \in \{\hat{\mathcal{P}}, \hat{\mathcal{S}}_r, \hat{\mathcal{K}}_r\}$ combined with Eqs. (1)–(4), (19), and (20).

For this constant control field, the storage efficiency is given by

$$\eta = \eta_C\left(1 - \frac{B\gamma_s}{J^2(1+r)}\right), \tag{30}$$

which approaches unity for $C \gg 1$ and $B \ll J^2/\gamma_s$. In Sec. VI, we extend this analysis to higher-bandwidth signals that operate beyond the adiabatic regime, where $\partial_t \hat{\mathcal{S}}_r = 0$ no longer holds.

The efficiency [Eq. (30)] and Eq. (26) exhibit interesting scaling with the parameter r for the adiabatic mapping. Defining new variables $\tau \equiv r\gamma_s(1+r)t$, $\hat{\mathcal{E}}^r_{\rm in} \equiv \hat{\mathcal{E}}_{\rm in}/[r\gamma_s(1+r)]$, and $\tilde{\gamma}^r_\Omega \equiv \tilde{\gamma}_\Omega/[\gamma_s(1+r)]$ renders Eq. (26) dimensionless:

$$\partial_\tau \hat{\mathcal{K}}_r = -\frac{\tilde{\gamma}^r_\Omega}{1+\tilde{\gamma}^r_\Omega}\left(\hat{\mathcal{K}}_r + i\sqrt{\frac{2C}{\tilde{\gamma}^r_\Omega(C+1)}}\hat{\mathcal{E}}^r_{\rm in}\right). \tag{31}$$

The resulting dimensionless parameter is $B\gamma_s/[J^2(1+r)] = B/[r\gamma_s(1+r)]$, which maintains the form of Eq. (30). In the limit $r \lesssim 1$, expanding to lowest order in r shows that the efficiency approximately retains its form under a rescaling of the pulse bandwidth $B/\gamma_s \to rB/\gamma_s$. This indicates that the memory can maintain high efficiency for small values of r, but with a reduced operational bandwidth that is approximately linear in r.

For completeness, we also present the expression for the output field, which describes the retrieval stage. Under the conditions in which Eq. (26) holds, the output field can be obtained by substituting Eqs. (5)–(25) into Eq. (1), along with the transformation in Eqs. (19) and (20), yielding

$$\hat{\mathcal{E}}_{\rm out} = \left(1 - 2\eta_C\frac{\gamma_s(1+r)}{\gamma_s(1+r)+\tilde{\gamma}_\Omega}\right)\hat{\mathcal{E}}_{\rm in} + i\sqrt{\frac{2\eta_C}{r\tilde{\gamma}_\Omega}}\frac{r(1+r)\gamma_s\tilde{\gamma}_\Omega}{\gamma_s(1+r)+\tilde{\gamma}_\Omega}\hat{\mathcal{K}}_r. \tag{32}$$

Equations (26) and (32) describe the adiabatic storage and retrieval processes between the signal and the dressed noble-gas operator. During the storage stage, $\langle\hat{\mathcal{E}}^\dagger_{\rm in}\hat{\mathcal{E}}_{\rm in}\rangle$ is nonzero and the signal acts as a source, mapping the signal onto the collective spin for storage. During retrieval, the decay of the dressed noble-gas operator corresponds to the conversion of collective spin excitations into retrieved photons (in the adiabatic limit and in the absence of other relaxation mechanisms) as shown by Eq. (32). The rate for this retrieval process, as captured by Eqs. (26) and (32) absent an input signal, is proportional to $\lambda = r(1+r)\gamma_s\tilde{\gamma}_\Omega/(\gamma_s(1+r)+\tilde{\gamma}_\Omega)$, satisfying $\lambda < (r+r^2)\gamma_s$. This slow retrieval rate for $r \ll 1$ highlights the inherently slow bandwidth of the retrieved signal in the adiabatic mapping.

V. MEMORIES BASED ON SPIN-EXCHANGE COLLISIONS

In this section, we briefly review key results of our recent analytical study on light storage in noble-gas spins via spin-exchange collisions [14], focusing on ultralow bandwidth and strong coupling configurations. This section provides background for the extensions presented in Sec. VI and facilitates comparison with memories based on metastability-exchange collisions.

A. Physical mechanism

Nuclear spins of noble-gas atoms can couple efficiently to spins of alkali-metal atoms via the Fermi contact interaction during spin-exchange collisions [12,13]. Since the spin precession angle during a single collision is small for many alkali-noble-gas pairs, the total precession of the collective spin accumulates coherently over many collisions, while noise and decoherence arising from the stochastic nature of the collisions remain minimal [13].

Unlike metastability-exchange collisions, where γ_k, J, and γ_s are interdependent through the parameter r, thereby limiting J and making γ_k non-negligible for practical applications, spin-exchange collisions with alkali-metal atoms allow J to exceed γ_s, enabling strong coherent coupling between the two species, as recently demonstrated [38]. Notably, for this configuration, γ_s accounts for all relaxation mechanisms of the alkali-metal atoms.[5] Furthermore, due to the weak collisional interactions between certain alkali-metal atoms and noble-gas spins (e.g., ^{3}He-K), the fundamental relaxation rate γ_k due to spin-exchange interactions can be exceptionally small (e.g., $\ll 1/\text{h}$) and, importantly, largely independent of J and γ_s. This opens possibilities for efficiently mapping much of the input signal onto the electron spin operator $\hat{\mathcal{S}}$, followed by efficient exchange with the noble-gas spins while dominating over electron-spin relaxation. Under ideal mapping conditions, excitations at the end of the process are stored solely in the noble-gas spins, allowing us to set $\hat{\mathcal{K}}_r = \hat{\mathcal{K}}$ in Eq. (9).

In Ref. [14], we derived Eqs. (2)–(4) for this system with $\xi = +1$ and analyzed two strategies that are efficient in two key limiting cases: low-bandwidth optical signals ($B \ll J^2/\gamma_s$) and high-bandwidth signals ($B \gg \gamma_s$ and $B \gtrsim J$). We now review the main results of Ref. [14], and in Sec. VI, study their optimality and extend to intermediate bandwidth regimes.

B. Adiabatic mapping

For low-bandwidth signals, under the conditions that $\hat{\mathcal{S}}$ evolves rapidly (compared with $\hat{\mathcal{K}}$) and the optical fields are slow ($B \ll J^2/(\gamma_s+\gamma_\Omega)$), one can set $\partial_t\hat{\mathcal{S}} = 0$ in Eq. (6). This yields the evolution of the collective noble-gas spin operator in Eq. (4):

$$\partial_t\hat{\mathcal{K}} = -(\gamma_k + \Gamma_J + i\bar{\delta}_k)\hat{\mathcal{K}} + a_J\hat{\mathcal{E}}_{\rm in}, \tag{33}$$

where

$$\Gamma_J(t) \equiv \frac{J^2}{\gamma_\Omega(t)+\gamma_s+i\bar{\delta}_s(t)} \tag{34}$$

and $a_J \equiv i\sqrt{\eta_C}\sqrt{2\gamma_\Omega}\Gamma_J/J$. Equation (33) has the same form as Eq. (27), thereby leading to a solution with the same functional form as Eq. (28).

To provide an analytical estimate, we consider the case of an exponentially shaped input pulse, where the optimal

[5] In the metastability-exchange configuration in Sec. IV, γ_s instead includes only the high relaxation rate associated with the metastability-exchange process, providing a lower bound for the actual relaxation of the optically accessible ensemble.

control field is given by a constant function with amplitude $\mathrm{Re}(\Gamma_J) = B$. In the limit $\gamma_k = 0$, the efficiency is given by

$$\eta_{\text{adiabatic}} = \frac{C}{C+1}\left(1 - \frac{B\gamma_s}{J^2}\right), \tag{35}$$

which resembles the form of Eq. (30).

C. Sequential mapping

For high-bandwidth signals, efficient storage is feasible when strong coupling is achieved. In the limit $J \gg \gamma_s$, a sequential storage scheme can be implemented, where light is first stored in the alkali-metal collective spin coherence and then transferred to the nuclear spins, following the sequence $\hat{\mathcal{E}}_{\text{in}} \to \hat{\mathcal{S}}(0) \to \hat{\mathcal{K}}(T')$. During the first stage, the electronic spins are excited resonantly ($\Delta = \bar{\delta}_s = 0$) at a rate $\gamma_\Omega = \mathrm{Re}(\Gamma_\Omega)$ [see Eq. (7)], similar to standard Λ-type memories [16]). Simultaneously, the noble-gas spins are decoupled from the dynamics by setting $\bar{\delta}_k \gg J$. For fast pulses, this stage can be approximately described by setting $\hat{\mathcal{K}} = 0$ in Eq. (6), resulting in the linear mapping between $\hat{\mathcal{S}}$ and the input light field:

$$\partial_t \hat{\mathcal{S}} = -(\gamma_s + \gamma_\Omega + i\bar{\delta}_s)\hat{\mathcal{S}} - \sqrt{\eta_C}\sqrt{2\gamma_\Omega}\hat{\mathcal{E}}_{\text{in}}, \tag{36}$$

whose solution has a similar form to Eq. (28).

During the second stage, the alkali and noble-gas spins are brought into resonance ($\bar{\delta}_s = \bar{\delta}_k = 0$), while the control field Ω is turned off, allowing the two spin species to efficiently exchange their quantum state after time $T' \approx \pi/(2J)$, akin to a π-pulse of the beamsplitter Hamiltonian [5]. As an example, for an exponentially shaped input pulse, the optimal control field during the first stage is a constant profile with amplitude $\gamma_\Omega = B$. In the limit $J \gg \gamma_s$, the storage efficiency is given by

$$\eta_{\text{sequential}} = \frac{C}{C+1}\frac{B}{B+\gamma_s}\exp\left(-\frac{\pi\gamma_s}{2J}\right), \tag{37}$$

where the exponential decay term accounts for the loss of excitations in the alkali-metal ensemble during the finite exchange time.

VI. NUMERICAL ANALYSIS

To extend the analytical results, we numerically optimized the storage protocols to maximize efficiency using an optimal-control approach following Ref. [39]. The optimization treated the temporal control field $\gamma_\Omega(t)$ and the detunings $\delta_s(t)$ and $\delta_k(t)$ as free parameters, aiming to maximize the storage efficiency η_∞ for given J/γ_s and B/γ_s. The equations of motion for the collective spin and field amplitudes were solved iteratively using a gradient-ascent algorithm with momentum until convergence. A full description of the cost functional, Lagrange multipliers, and numerical update procedure is provided in Appendix C. A similar approach, though beyond the scope of this work, could also be applied to optimize retrieval efficiency into a specific target mode.

In Fig. 2, we present the reduced efficiency parameter η_∞ for the numerically optimized control fields across different values of B/γ_s and J/γ_s. Figure 2(a) shows the results for metastability-exchange collisions ($\xi = -1$). While we present the model results for $J < \gamma_s$ (i.e., $r < 1$) to focus on higher-bandwidth signals, we emphasize that, in practical experimental conditions, this configuration often requires $r \ll 1$, which consequently enforces $J \ll \gamma_s$. Figure 2(b) displays the storage efficiency for the case of spin-exchange collisions ($\xi = +1$).

The optimization shows that efficient storage of light is obtained for low-bandwidth signals $B < \gamma_\Omega, J^2/\gamma_s$, as expected from the adiabatic mapping. For storage based on spin-exchange collisions, we find that efficient storage can be realized for any $J \gg \gamma_s$ as expected in the strong-coupling regime. We find numerically that the optimal value of δ_s is near zero. We discuss the optimal value of δ_s and its dependence on the signal phase in Appendix E.

We compare the numerically optimized efficiency with the one associated with the simple analytical schemes in Secs. IV and V, whose efficiencies are given in Eqs. (30), (35), and (37). In Fig. 2(c), we present the positive values of the storage efficiency in Eq. (30) for storage based on metastability-exchange collisions, and in Fig. 2(d), the maximal storage efficiency of Eqs. (35) and (37) for storage based on spin-exchange collisions. Interestingly, the analytic expressions for the spin-exchange configuration provide a good approximation to the numerically optimized efficiency even away from their validity limits, especially for the spin-exchange case. For metastability-exchange collisions, on the other hand, the numerical solution is similar to the analytic solution at low pulse bandwidths, but displays remarkably higher efficiencies at large bandwidth far from the adiabatic regime, owing to a better performance of optimal nonadiabatic solutions. Similar behavior has been observed in Ref. [39], where numerically optimized solutions were shown to dramatically increase the memory bandwidth.

The similarity between the analytical and numerical efficiency maps suggests that the numerically optimized solutions may resemble the analytical ones. To explore this, in Fig. 3(a), we present the maximal excitation of the electronic spin at intermediate times during the storage process, $\max_t(\mathcal{S}^*(t)\mathcal{S}(t))$ for spin-exchange collisions ($\xi = +1$). Strikingly, we find that, in most of the parameter space, the collective electron spin is either nearly unexcited or temporarily holds a significant portion of the input excitations from the signal field, which are mapped directly onto the electrons. Dashed white lines indicate the 10% and 90% excitation values, respectively. In Figs. 3(b) and 3(c), we plot two of the numerically optimized solutions, representing the blue diamond and red circle symbols in Fig. 3(a), respectively. In Fig. 3(b), we find that the numerically optimized solution is nearly identical to the sequential scheme, where the excitation is first mapped onto the alkali-metal spins, and only later mapped to the noble-gas spins in the absence of a control field. In Fig. 3(c), the numerically optimized solution is similar to the adiabatic scheme, where the control field is constantly on, and the electron spins are nearly unexcited. The solutions between the two dashed lines in Fig. 3(a) belong to neither of these schemes, yet could attain high efficiency. Examples of these solutions are plotted in Fig. 6.

We repeat the preceding analysis for the $\xi = -1$ case, as shown in Figs. 3(d)–3(f). For low-bandwidth signals, we find that numerically optimized solutions attain the form of the adiabatic scheme. For high-bandwidth signals, we find that

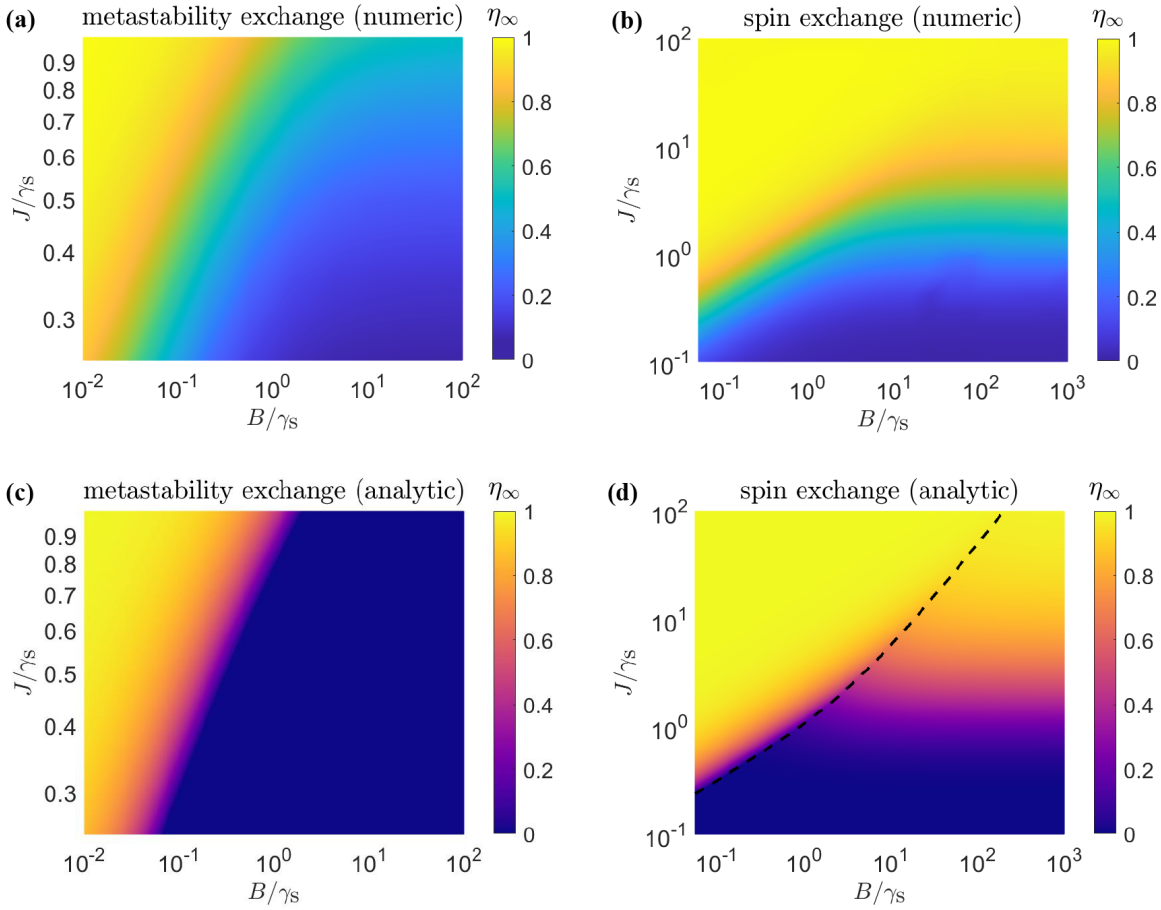

FIG. 2. Numerically optimized storage efficiency. We present the attained efficiency of the storage sequences for (a) metastability-exchange collisions ($\xi = -1$) and (b) spin-exchange collisions ($\xi = +1$). The color scale shows the storage efficiency η_∞ in the large-cooperativity limit. Here, J is the fixed, magnetic-like coupling rate. The limited range of J/γ_s in panel (a) compared with panel (b) originates from the different nature of the exchange processes. See text and Sec. C 2 for details of the numerical optimization protocol. Maximal efficiency of the analytical sequences presented in Secs. IV and V, corresponding to Eq. (30) in panel (c) and Eqs. (35)–(37) in panel (d). Dashed line in panel (d) indicates the boundary at which the storage sequence changes from adiabatic to sequential. Despite the similarity in form between metastability exchange and spin exchange, achieving high efficiency requires relatively large values of r. At $r \ll 1$, where most metastability-exchange experiments operate, the bandwidth must be rescaled approximately linearly with r to maintain efficiency [see text and Eq. (31)].

the solutions are nonadiabatic and involve increased electronic spin population, yet show moderate efficiency owing to the restrictive ratio of J/γ_s that can be physically realized using the metastability-exchange mechanism.

VII. DISCUSSION

The storage efficiencies of noble-gas spins based on metastability-exchange collisions or spin-exchange collisions can theoretically approach unity for large cooperativity ($C \gg 1$) and sufficiently low pulse bandwidth $B \ll \gamma_s$. In the limit of zero bandwidth ($B \ll J^2/\gamma_s$), the storage efficiency of the adiabatic scheme approaches $C/(C+1)$, which is the maximal efficiency of optically accessible Λ-type memories. For these scenarios, we find that the numerically optimal sequences follow adiabatic-like protocols, where the electron spins remain nearly unexcited, and the optical control field Ω is kept high throughout the pulse.

For higher pulse bandwidth ($B \gtrsim \gamma_s$), it is optimal to transfer a significant part or even most of the excitation to the electronic spins first, and then reduce the power of the optical control field during the transfer of excitation from the electronic spins to noble-gas spins. While configurations based on spin-exchange collisions can remain efficient if the exchange coupling is sufficiently large ($J \gtrsim \gamma_s$), the efficiency of metastability-exchange configurations is more limited owing to the physical limitation on the exchange-rate strength relative to the accompanying relaxation.

Both configurations examined in this work are experimentally feasible. Control of Rabi frequency Ω and detuning δ_s is implemented by tuning the control laser power and frequency, respectively, whereas the difference $\delta_k - \delta_s$ can be controlled by an external magnetic field owing to the different magnetic dipole moments (gyromagnetic ratios) of the electron and nuclear spins [11,14]. For the metastability-exchange-based configuration, using the parameters from Ref. [11] and taking $r = 10^{-6}$, storage of low-bandwidth signals can be implemented efficiently. We estimate a typical bandwidth for this scheme to be limited by $B \lesssim (2\pi)\,1\,\mathrm{Hz}$, e.g., with efficiency $\eta_{tot} \approx 0.76$ for a bandwidth of $(2\pi)\,0.1\,\mathrm{Hz}$, where

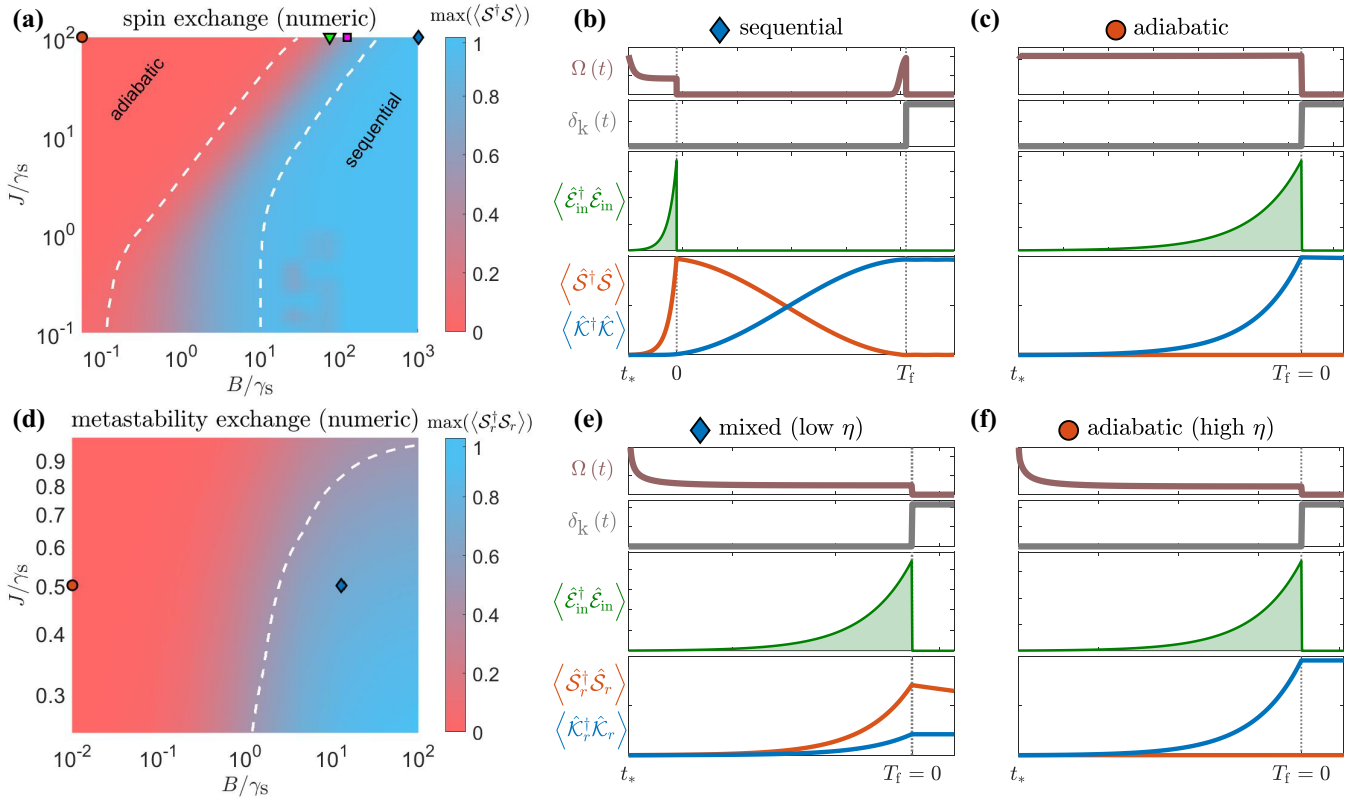

FIG. 3. Optimal storage sequences. Maximal excitation $\langle\hat{\mathcal{S}}^\dagger\hat{\mathcal{S}}\rangle$ of the electron spins during the storage sequence for the numerically optimized solutions for spin-exchange collisions (a) and metastability-exchange collisions (d). Two distinct regimes of nearly complete excitation (blue) or nearly no excitation (red) are observed for the optimal solutions as a function of the bandwidth B and coupling strength J. Dashed lines denote the condition(s) $\max(\langle\hat{\mathcal{S}}^\dagger\hat{\mathcal{S}}\rangle) = 0.9$ and $\max(\langle\hat{\mathcal{S}}^\dagger\hat{\mathcal{S}}\rangle) = 0.1$ in panel (a) and $\max(\langle\hat{\mathcal{S}}^\dagger\hat{\mathcal{S}}\rangle) = 0.5$ in panel (d), marking the approximate boundaries of these two regimes, qualitatively showing where the optimal solutions follow the adiabatic or sequential strategies. (b), (c) Particular numerically optimized solutions, corresponding to the blue diamond and red circle in panel (a), indicating sequential-like and adiabatic-like storage strategies, respectively. (e), (f) Particular numerically optimized solutions corresponding to the blue diamond and red circle in panel (d), indicating solutions with different bandwidth and different electron excitation, where panel (f) follows an adiabatic solution (see Appendix IV). The optimization parameters used in panels (a) and (d) are identical to the ones presented in Figs. 2(a) and 2(b), respectively. We find that $\delta_s(t)$ (not shown) is near zero throughout the storage sequence, a result of the constant phase of the input pulse, as we discuss in Appendix E. The increase in Ω toward the end of the storage sequence in panel (b) is merely an artifact of the optimizer trying to decouple the alkali and noble-gas spins more efficiently, as there is no constraint on the control field amplitude in the optimization. Intermediate bandwidth solutions corresponding to the green triangle and the magenta square in panel (a) are shown in Fig. 6.

$\eta_{\text{tot}} \approx \eta^2$ is the approximate combined memory efficiency of the storage and retrieval stages [14,16]. Because the typical B for efficient solutions with $r \ll 1$ is very low for most memory applications, our numerical analysis focuses on higher values of r, with scaling to lower values of r determined using Eq. (31). Therefore, experimental realizations may need to operate at higher r to achieve efficient, high-bandwidth memories. For the spin-exchange-based configuration, we consider a mixture of potassium and helium-3. For high-bandwidth pulses, we estimate $B \gtrsim (2\pi)$ 1 MHz and efficiency of $\eta_{\text{tot}} \approx 0.89$ using the sequential strategy, whereas, for very low-bandwidth pulses ($B \lesssim (2\pi)10$ Hz), even higher efficiencies $\eta_{\text{tot}} \approx 0.94$ can be realized with the adiabatic scheme. We summarize these results in Table I. We assume that, during the long memory time, the relaxation of the noble-gas spins by coupling to the electronic spins is suppressed. In metastability-exchange collisions, this can be implemented by turning off the discharge, which leaves the entire noble-gas population in the electronic ground-state manifold (with the optical signal mapped onto the spin states). For spin-exchange collisions, turning off can be realized by first turning off the optical pumping beam, which leaves only spin-rotation coupling. The latter can then be suppressed by cooling the cell and reducing the alkali-atom vapor density through condensation. Owing to the large separation of scales between γ_k and γ_s, we set the former to zero in all the calculations performed in this work involving spin-exchange collisions.

Multiple excited and ground sublevels in both metastable helium and alkali-metal atoms can modify memory dynamics and generate noise photons through competing processes such as four-wave mixing [3,42–45]. In this work, we adopt a simplified description in which the alkali-metal atoms and metastable helium are treated as effective Λ-type systems, and couplings to additional levels are neglected. This reduction is valid when the excitation bandwidth and the generalized Rabi

TABLE I. Estimation of feasible experimental parameters. The parameters are adapted from the provided references, and the efficiencies are computed from Eqs. (30)–(37), for the second configuration taking the maximal values of the parameter range and estimating the total memory efficiency using $\eta_{\rm tot} \approx \eta^2$. †, ∗ denote configurations in which the exchange interaction is turned on or off, respectively. It is assumed that, during the memory time, following the storage, the exchange interaction is turned off (see text).

Platform	γ_s $[(2\pi)\,\mathrm{Hz}]$	J $[(2\pi)\,\mathrm{Hz}]$	J/γ_s	C	$1/\gamma_k$	Time-bandwidth product, B/γ_k	Efficiency, $\eta_{\rm tot}$
Metastable and ground-state helium-3	5×10^6 [11]	5×10^3 [11]	10^{-3}	500 [11]	$0.2^\dagger$ s [11] 100^* h [40]	$\sim 10^5$	76% | adiabatic | $B\sim 0.1\ (2\pi)$Hz
Alkali-noble-gas mixture	6−15 [14,41]	490−690 [14,38]	33−115	37 [14]	$2^\dagger$ h [38] 100^* h [40]	$\gtrsim 10^{10}$	94% | adiabatic | $B \lesssim 10\ (2\pi)$Hz 89% | sequential | $B \gtrsim$ 1 (2π)MHz

frequency (including detuning) are both much smaller than the excited-state energy-level separation, a regime that supports electromagnetically induced transparency (EIT)- and Raman-based memories [3,21] for either metastability-exchange or spin-exchange operation, provided the buffer gas pressure is kept low to avoid pressure broadening. Coupling to other levels can still impact performance; several strategies have been developed to suppress such channels in related settings [46–49]. In the far-off-resonant limit, where the detuning exceeds the hyperfine splittings and the optical linewidth, the light couples predominantly to the electron spin and the level structure is well captured by an effective four-level (double-Λ) configuration with two ground and two excited spin states [5,50]. The multipass schemes of Refs. [51,52] suppress one of the two Λ pathways as well as four-wave mixing, thereby isolating a single-Λ memory consistent with the model used here. These schemes are anticipated to remain effective in the presence of buffer gas, although this has not yet been verified experimentally. For noble-gas nuclei with spin-1/2, whose coupling to alkali spins is predominantly isotropic via the Fermi contact interaction [7], the dominant noise originates from the alkali-metal ensemble. In Ref. [14], we analyzed additional noise sources, including imperfect spin polarization and fluorescence, and identified conditions under which their contributions are negligible; those conclusions are expected to apply in the present configuration as well.

It is interesting to compare our results with the optimal storage strategy for electron spins in a Λ-type system [16]. The latter exhibits adiabatic-like optimal solutions, achieved by shaping the control fields over time to support high-bandwidth pulses. Since the exchange interaction strength is fixed and cannot be modulated over time to match the input pulse shape, the optimal strategy deviates from the adiabatic scheme for higher pulse bandwidths. In this case, the excitations are temporarily stored—either fully or partially—on the electronic spins, in contrast to the adiabatic strategy, where the electronic spins remain only weakly excited. The strong coupling regime is particularly promising from an application perspective, offering an avenue to realize high-time-bandwidth-product memories. The time-bandwidth product is one of the main figures of merit for optical quantum memories [1], defined as the product of the pulse bandwidth and the memory coherence time. For noble-gas spins, the coherence time can be exceptionally long ($1/\gamma_k \gtrsim 1$ h), underscoring the remarkable potential of this technology.

ACKNOWLEDGMENTS

E.R., R.S., E.P., and O.F. acknowledge financial support by the Israel Science Foundation, the US-Israel BSF and US NSF, the Pazy Foundation, the Minerva Foundation with funding from the Federal German Ministry for Education and Research, the Estate of Louise Yasgour, and the Laboratory in Memory of Leon and Blacky Broder. A.V.G. was supported in part by DARPA SAVaNT ADVENT, ARL (W911NF-24-2-0107), ARO MURI, AFOSR MURI, ONR MURI, AFOSR, NSF STAQ program, DoE ASCR Quantum Testbed Pathfinder program (Awards No. DE-SC0019040 and No. DE-SC0024220), NSF QLCI (Award No. OMA-2120757), and NQVL:QSTD:Pilot:FTL. A.V.G. also acknowledges support from the U.S. Department of Energy, Office of Science, Accelerated Research in Quantum Computing, Fundamental Algorithmic Research toward Quantum Utility (FAR-Qu). O.K. and A.V.G. also acknowledge support from the U.S. Department of Energy, Office of Science, National Quantum Information Science Research Centers, Quantum Systems Accelerator (QSA).

DATA AVAILABILITY

The data that support the findings of this article are not publicly available. The data are available from the authors upon reasonable request.

APPENDIX A: METASTABILITY-EXCHANGE EQUATIONS OF MOTION

In this Appendix, we describe the correspondence between the notation used for the dynamics of collective operators in Ref. [11] and the notation used in Eqs. (2)–(4).

In Ref. [11], the dynamics of the proposed metastability-exchage-based memory is described in Eqs. (2)–(5) therein. We can relate the notation in Ref. [11] to our notation as

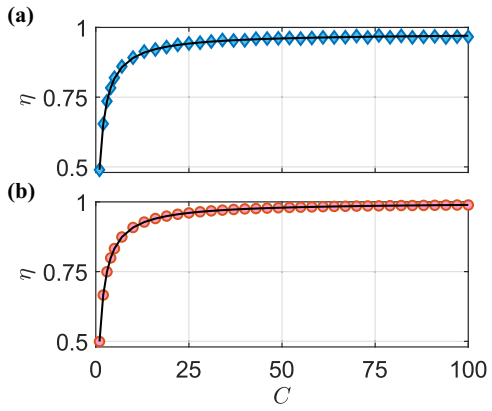

FIG. 4. Numerical verification of the scaling with C. The factorization $\eta = \eta_\infty C/(C+1)$ (black line) is verified numerically (light blue diamond and light red circle) for two configurations: (a) $B/\gamma_s = 10^3$ [corresponding to the blue diamond in Fig. 3(a)] and (b) $B/\gamma_s \approx 5.62 \times 10^{-2}$ [corresponding to the red circle in Fig. 3(a)], both taken at $J/\gamma_s = 100$.

follows: the field $\hat{\mathcal{E}}_{in} \equiv \hat{A}_{in}$ and coherences $\hat{\mathcal{P}} \equiv -\hat{S}_{23}/\sqrt{n}$, $\hat{\mathcal{S}} \equiv \hat{S}_{21}/\sqrt{n}$, $\hat{\mathcal{K}} \equiv i\hat{I}_{09}/\sqrt{N}$. Additionally, the rates map as $\gamma_p \equiv \gamma$, $\gamma_s \equiv \gamma_m$, $\gamma_k \equiv \gamma_f$, $\delta_s \equiv -\delta$, and $\delta_k \equiv -\delta_I$, where n and N denote the number densities in the metastable and ground state, respectively, using the notation from Ref. [11] (not to be confused with N representing the number of photons in the pulse in the rest of this work). We also define $J \equiv \sqrt{\gamma_s \gamma_k}$ and assume Ω is real. Notably, unlike the model in Sec. V, which includes, and is limited by, relaxation processes whose mechanism is unrelated to the underlying exchange interaction; here, the metastability-exchange interaction itself generates nonzero relaxation. Adopting the assumptions in Ref. [11], we consider only these relaxation rates in this model and neglect all other spin relaxation mechanisms that are not associated with the metastability-exchange interaction.

APPENDIX B: SCALING LAW OF STORAGE EFFICIENCY

We numerically verify the dependence of the numerically optimized efficiency on the cooperativity for two distinctively different points of the spin-exchange configuration. In Fig. 4, we present the numerically attained efficiency for each value of C compared with the scaled efficiency calculated at $C = 100$, showing excellent agreement.

APPENDIX C: NUMERICAL OPTIMIZATION FRAMEWORK AND ROUTINE

This Appendix provides the full description of the optimal-control method used to maximize the storage efficiency presented in Sec. VI.

1. Optimization framework

Focusing on memory efficiency, we follow the approach in Refs. [16,28], replacing the quantum operators with complex time-dependent functions $\hat{\mathcal{S}} \to \mathcal{S}$, $\hat{\mathcal{K}} \to \mathcal{K}$, and $\hat{\mathcal{E}}_{in} \to \mathcal{E}_{in}$. We assume the spin ensembles are initially in a vacuum state, with no initial excitations. For spins, these functions represent the tilt (displacement) of the coherent spin state, while for light, they describe the field displacement for coherent states and define the temporal pulse shape. Although this method does not fully characterize the quantum state of the stored and retrieved photons, it enables the assessment of storage efficiency for general photonic signals by evaluating the output energy or number of stored excitations.

We adopt the optimal-control framework of Ref. [39] and numerically solve Eqs. (4) and (6). We set $\Delta = 0$ and real Ω (such that $\phi_\Omega = 0$), as these parameters do not independently affect the memory efficiency in Eq. (17). For the spin-exchange configuration, we further set $\gamma_k = 0$ and $\xi = +1$, while for the metastability-exchange configuration, we take $\xi = -1$ and $\gamma_k/\gamma_s = r$, where r is determined by the relation $J/\gamma_s = \sqrt{r}$. Thus, the parameter space of the normalized storage efficiency $\eta_\infty = \eta/\eta_C$ that we study in this work is spanned by two independent dimensionless parameters J/γ_s and B/γ_s [see Eq. (17)].

The input pulse $\mathcal{E}_{in}(t)$ spans from $t = t_* < 0$ to $t = 0$. We use the gradient ascent method to optimize the temporal profiles of $\Omega_N(t) \equiv \sqrt{\gamma_\Omega(t)} = \Omega(t)/\sqrt{\gamma_p(1+C)}$ (N for normalized) as well as $\delta_s(t)$ and $\delta_k(t)$ given the parameters B/γ_s and J/γ_s to maximize the storage efficiency. For storage based on metastability-exchange collisions, we compute the normalized efficiency as $\eta_\infty = \max_s(\langle \hat{\mathcal{K}}_r(s)^\dagger \hat{\mathcal{K}}_r(s)\rangle)/\eta_C$ for $s \leqslant T'$, where $T' = 4/(\gamma_s + \gamma_k)$ and $\hat{\mathcal{K}}_r$ is given in Eq. (20). For storage based on spin-exchange collisions, we compute $\eta_\infty = \max_s(\langle \hat{\mathcal{K}}(s)^\dagger \hat{\mathcal{K}}(s)\rangle)/\eta_C$. We take $s \leqslant T'$, where $T' = \pi/[2\max(\sqrt{J^2 - \gamma_s^2/4}, \gamma_s)] \gtrsim 0$, to enable operation in the sequential scheme, which requires this duration [14]. Since the input signal starts at $t = t_*$ and ends at $t = 0$, choosing $T' \geqslant 0$ allows for additional interaction between the spin operators $\mathcal{S}$ and $\mathcal{K}$ after the optical signal has ended.

2. Optimization routine

We numerically vary the control functions between different iterations following Ref. [39], aiming to maximize the functional

$$\Phi = \frac{\eta}{2} - \frac{1}{2}\int_{-\infty}^{T'} dt\big[k^*(\partial_t \mathcal{K} + (\gamma_k + i\delta_k)\mathcal{K} + i\xi J\mathcal{S}) + s^*(\partial_t \mathcal{S} + (\gamma_s + \Omega_N^2 + i\delta_s)\mathcal{S} + iJ\mathcal{K} + \sqrt{2\eta_C \Omega_N}\mathcal{E}_{in}) + \text{H.c.}\big], \tag{C1}$$

where $k(t)$ and $s(t)$ are the Lagrange multipliers, which ensure that Eqs. (4) and (6) for $\mathcal{K}$ and $\mathcal{S}$ are satisfied. For solution satisfying the equation of motion, the integrand in Eq. (C1) vanishes. Variational calculus yields the equations of motion for the Lagrange multipliers:

$$\partial_t s = (\gamma_s + \gamma_\Omega - i\delta_s)s - i\xi Jk, \tag{C2}$$

$$\partial_t k = (\gamma_k - i\delta_k)k - iJs. \tag{C3}$$

The conditions at $t = T'$ are given by $s(T') = 0$ and $k(T') = \mathcal{K}(T')$ for $\xi = +1$, and by $s(T') = -i\sqrt{\frac{r}{1+r}}\mathcal{K}_r(T')$ and $k(T') = \frac{1}{\sqrt{1+r}}\mathcal{K}_r(T')$ for $\xi = -1$ based on the transformation in Eqs. (19) and (20).

We are interested in computing the multipliers $s(t)$ and $k(t)$ for $t \leqslant T'$, and therefore we numerically solve Eqs. (C2)–(C3) backwards in time from $t = T'$. In every iteration, we first solve Eqs. (4) and (6), compute $\mathcal{K}(T')$, and then solve Eqs. (C2)–(C3). We use these solutions to calculate the functional derivatives of the control functions $\Omega_{\rm N}(t)$, $\delta_{\rm s}(t)$, and $\delta_{\rm k}(t)$:

$$\frac{\partial \Phi}{\partial \Omega_{\rm N}} = -2\Omega_{\rm N}\mathrm{Re}(s^*\mathcal{S}) - \sqrt{2\eta_C}\mathrm{Re}(s)\mathcal{E}_{\rm in}, \tag{C4}$$

$$\frac{\partial \Phi}{\partial \delta_{\rm s}} = \mathrm{Im}(s^*\mathcal{S}), \tag{C5}$$

$$\frac{\partial \Phi}{\partial \delta_{\rm k}} = \mathrm{Im}(k^*\mathcal{K}). \tag{C6}$$

This set of equations is used to update the control functions for the next iteration. The control functions in the nth iteration are determined using the gradient ascent method with momentum [53,54]:

$$\Omega_{\rm N}^{(n)} = (1+\alpha_n)\Omega_{\rm N}^{(n-1)} - \alpha_n\Omega_{\rm N}^{(n-2)} + \frac{1}{\lambda_{\Omega_{\rm N}}}\frac{\partial \Phi}{\partial \Omega_{\rm N}}, \tag{C7}$$

$$\delta_{\rm s}^{(n)} = (1+\alpha_n)\delta_{\rm s}^{(n-1)} - \alpha_n\delta_{\rm s}^{(n-2)} + \frac{1}{\lambda_{\delta_{\rm s}}}\frac{\partial \Phi}{\partial \delta_{\rm s}}, \tag{C8}$$

$$\delta_{\rm k}^{(n)} = (1+\alpha_n)\delta_{\rm k}^{(n-1)} - \alpha_n\delta_{\rm k}^{(n-2)} + \frac{1}{\lambda_{\delta_{\rm k}}}\frac{\partial \Phi}{\partial \delta_{\rm k}}. \tag{C9}$$

Here, we choose $\alpha_n = 0.9$ for $n \geqslant 3$ and $\alpha = 0$ otherwise, and use λ to denote the inverse step size between iterations.

We found the following numerical procedure to be efficient. For each optimization run, we first set $\delta_{\rm s}(t) = \delta_{\rm k}(t) = 0$ and optimize solely with respect to $\Omega_{\rm N}(t)$. The step size $\lambda_{\Omega_{\rm N}}$ is chosen within the range $[10^{-2}, 10^{2}]$, with smaller B corresponding to smaller values of $\lambda_{\Omega_{\rm N}}$. The initial guess for $\Omega_{\rm N}(t)$ in the run with the maximal value of $J = J_{\max}$ for each B is a constant (square) pulse for $t \leqslant T'$. For smaller values of $J < J_{\max}$, we attempt two independent optimization procedures using different initial guesses based on the optimal solution $\Omega_{\rm N,iter,1}(t)$ previously computed for the same B and nearest J. One guess is $\Omega_{\rm N,iter,1}(t)$ up to the time at which $\mathcal{K}$ is maximal, with additional padding of zeros at the end of the pulse to account for the increase of T' due to the decrease of J. The other guess is a square pulse taking the average value of $\Omega_{\rm N,iter,1}(t)$ over the time range $t_*/2 \leqslant t \leqslant 0$, where the simulation starts at $t_* < 0$. We note that the efficiency is generally insensitive to the early shape of the control field, assuming that at t_*, the signal begins near zero and contains a negligible fraction of the control excitation. For each value of J and B, we record the initial guess $\Omega_{\rm N,iter,2}(t)$ as the solution that realizes the higher storage efficiency of the two optimization attempts. It is worth mentioning that when $\Omega_{\rm N}^2 = \gamma_\Omega \gg J$, the alkali and nuclear spins are effectively decoupled, meaning that $\Omega_{\rm N}^2 = \gamma_\Omega$ can fulfill the role of δ_k in the initial optimization step. After this, in the spin-exchange case, we allow the solver to vary $\delta_{\rm s}(t)$ and $\delta_{\rm k}(t)$ in addition to $\Omega_{\rm N}(t)$. The step sizes are chosen adaptively: $\lambda_{\delta_{\rm s}}^{(n)} = \mathrm{mean}(\gamma_\Omega)^{-1}$ and $\lambda_{\delta_{\rm k}}^{(n)} = \mathrm{mean}(\gamma_J)^{-1}$, where $\Omega_{\rm N}^2(t) = \gamma_\Omega(t)$ and $\gamma_J(t) \equiv \mathrm{Re}(\Gamma_J)$ correspond to the values obtained from the previous optimization iteration for $\Omega_{\rm N}^{(n-1)}(t)$.

We typically observe convergence in the computed η_∞ after approximately 5000 iterations at $J = J_{\max}$, whereas for $J < J_{\max}$ convergence is generally faster since the initial condition is already close to the optimum. We also test different initial conditions, including high values of $\delta_{\rm k}$ for the duration of the input field. The shapes of $\delta_{\rm k}$ and $\delta_{\rm s}$ have only a minor influence on the efficiency, except at the point when the control field $\Omega_{\rm N}^2(t) = \gamma_\Omega(t)$ is turned off, where complete decoupling between the spin ensembles is necessary, such as after storage. In such cases, a large $\delta_{\rm k}$ enables effective suppression of the coupling to the electronic spins.

We run the simulations for three input pulse profiles: exponentially shaped, Lorentzian, and Gaussian. In this section, we present the results for the exponentially shaped pulse profile and compare it with the other two profiles at similar bandwidths in Appendix D. For the exponentially shaped pulse, we consider the temporal profile

$$\mathcal{E}_{\rm in}(t) = A\sqrt{\frac{2}{T}}e^{t/T}, \quad t_\star \leqslant t \leqslant 0, \tag{C10}$$

and zero otherwise, setting $T = B^{-1}$. For Λ-type memories operating in the adiabatic regime, optimal storage of an exponentially shaped signal (with $t_\star = -\infty$) is achieved using a square control pulse [16]. This choice allows for a direct comparison with analytical expressions for storage efficiencies given in Secs. IV and V. To reduce numerical complexity, we truncate the pulse at $t_\star = -3T$, ensuring that the integral $\int_{-3T}^{0}|\mathcal{E}_{\rm in}(t)|^2dt = 1$ is satisfied by setting $A = e^3/\sqrt{e^6-1}$. The overlap fidelity between the truncated pulse and its ideal form is $\mathcal{F} = |\int_{-\infty}^{0}\mathrm{d}t\ \mathcal{E}^*(t,t_\star)\mathcal{E}(t,t_\star=-\infty)|^2 = A^{-2}$, which exceeds 99%, ensuring that the numerical truncation introduces a negligible error.

APPENDIX D: ROBUSTNESS TO DIFFERENT TEMPORAL SIGNALS

In this Appendix, we verify, for $\xi = +1$, the robustness and applicability of our results to different pulse shapes. For that purpose, we have numerically tested optimal storage of light for different pulse shapes at several different system parameters. In Fig. 5, we present the control fields and efficiencies for two cases corresponding to the parameters of the red circle and blue diamond in Fig. 3(a). We compare the exponential pulse with Gaussian and Lorentzian pulses of similar bandwidth, given by the following expressions:

$$\mathcal{E}_{\rm in}(t) = A\frac{1}{(2\pi T^2)^{\frac{1}{4}}}\exp\left(-\frac{(t-t_*/2)^2}{4T^2}\right), \quad T = \frac{\sqrt{2\ln 2}}{2}B^{-1}, \tag{D1}$$

$$\mathcal{E}_{\rm in}(t) = A\sqrt{\frac{2}{\pi T}}\frac{T^2}{T^2+(t-t_*/2)^2}, \qquad T = \frac{\ln 2}{2}B^{-1}, \tag{D2}$$

where $t_\star \leqslant t \leqslant 0$ and A is a normalization constant that depends on the specific pulse shape (the value in the main text is for an exponentially shaped pulse). Both pulses are truncated symmetrically [see top row in Figs. 5(a) and 5(b)], and we choose t_* such that the pulses have a 99% overlap with the ideal (nontruncated) pulse shape, similar to the exponential pulse shape presented in Eq. (C10). For this test, we have optimized over γ_Ω, without the additional step of optimizing over $\delta_{\rm s}$ and $\delta_{\rm k}$ as done for the exponential pulse, setting the latter to

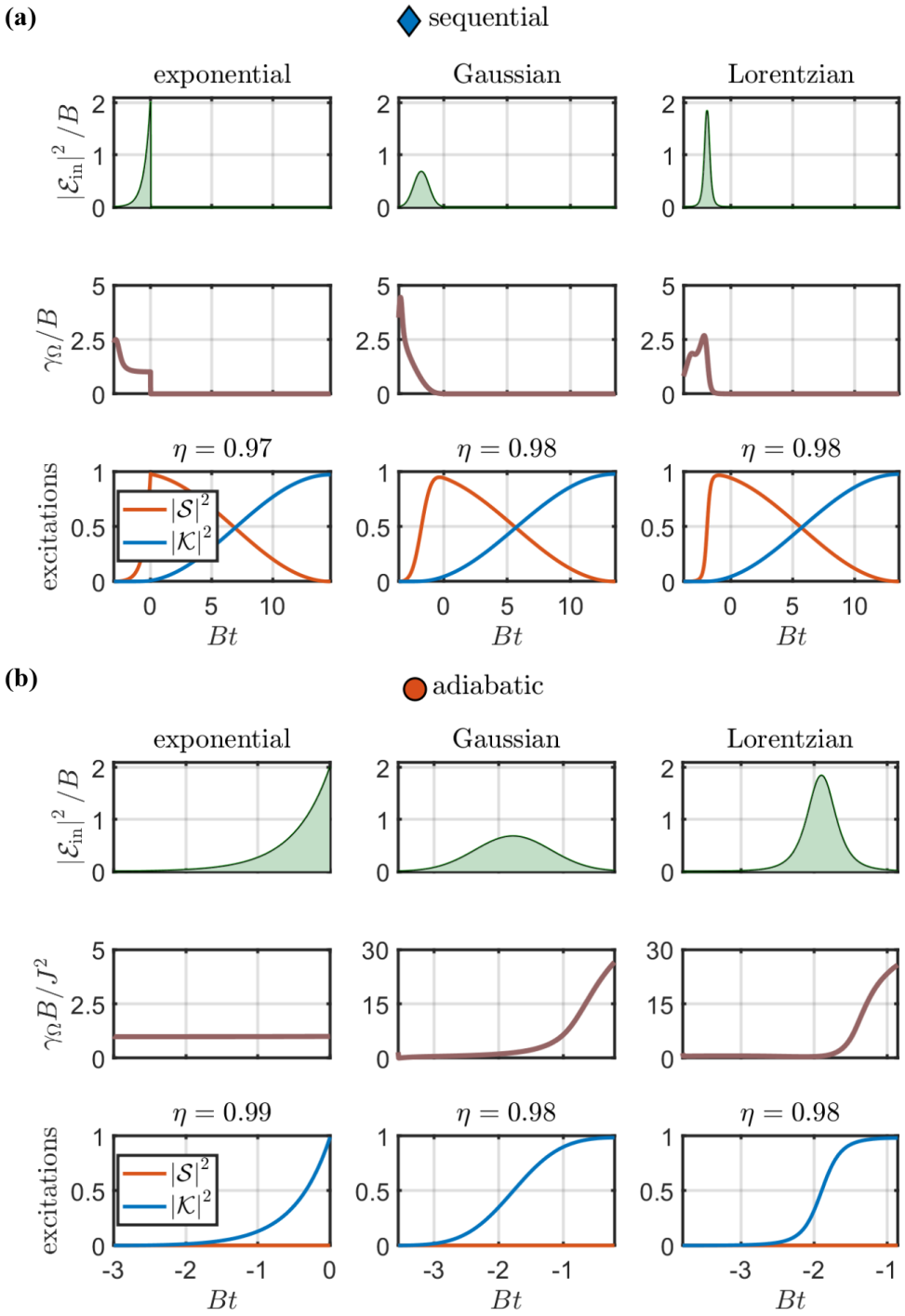

FIG. 5. Numerical optimization for storage of exponential, Gaussian, and Lorentzian pulse shapes with bandwidth $2B$ for the spin-exchange configuration ($\xi = +1$). (a) $J/\gamma_s \approx 100$ and $B/\gamma_s \approx 10^3$, corresponding to the blue diamond in Fig. 3(a). (b) $J/\gamma_s \approx 100$ and $B/\gamma_s \approx 5.62 \times 10^{-2}$, corresponding to the red circle in Fig. 3(a). Top: optical signal. Middle: optical control field (a parameter proportional to its intensity). Bottom: The efficiencies differ between different pulse shapes by no more than 1%.

zero. This step can be justified by the observation that $\gamma_\Omega > J$ decouples alkali and nuclear spins similarly to δ_k, as apparent in all numerical solutions in this Appendix. We furthermore truncate the solution at time T_f where the storage efficiency is maximal [resulting, e.g., in the asymmetry of the Lorentzian curve in Fig. 5(b)]. Except for different temporal shaping of the control fields, we find similar performance for different pulses. The predicated values for the efficiencies, calculated using Eqs. (30) and (37), $\eta_{\rm sequential} = 97\%$ and $\eta_{\rm adiabatic} = 99\%$, respectively, are within 1% of the values obtained from optimization.

APPENDIX E: OPTIMAL δ_s

In this Appendix, we analyze the dependence of the sequential and adiabatic storage schemes on δ_s for the spin-

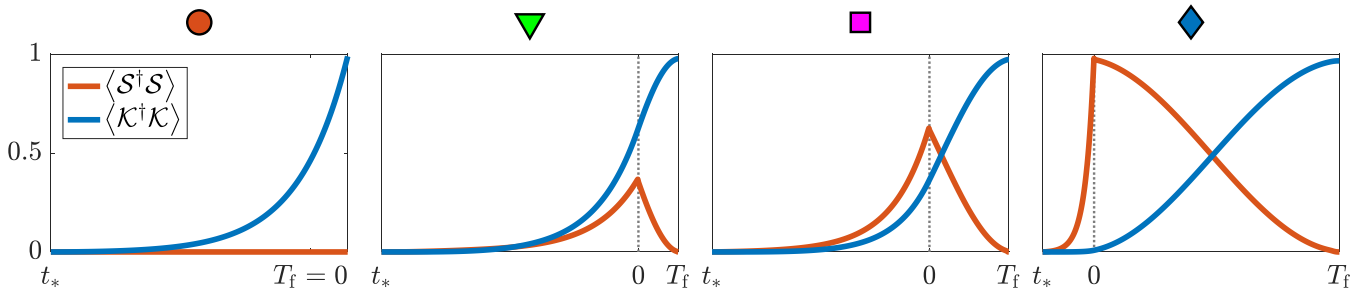

FIG. 6. Intermediate solutions in spin-exchange-based memories. We show the dynamics of the alkali-metal $\langle \hat{\mathcal{S}}^\dagger \hat{\mathcal{S}} \rangle$ (red) and noble-gas $\langle \hat{\mathcal{K}}^\dagger \hat{\mathcal{K}} \rangle$ (blue) collective spin excitations in the strong-coupling regime, for the spin-exchange based configuration. The spins are driven by the numerically optimized control fields for an exponentially shaped input pulse, as one traces a line in parameter space, from adiabatic to sequential regime. The different graphs correspond to the markers in Fig. 3(d).

exchange configuration to highlight its role in the storage process. We show analytically that $\delta_s = 0$ is optimal for both the sequential and adiabatic schemes, consistent with our numerical finding that $\delta_s = 0$ remains optimal across the explored parameter space. In the sequential scheme, under the assumption that the noble-gas spins are decoupled ($|\delta_k - \delta_s| \gg J$) in the first stage of the storage ($\mathcal{E}_{in} \to \mathcal{S}$), the spin coherence is given by [14,16]

$$\mathcal{S}(0) = \int_{-\infty}^{0} h_\Omega(t)\mathcal{E}_{in}(t)\mathrm{d}t. \tag{E1}$$

Here, the transfer function is $h_\Omega(t) = -Q\Omega^* e^{-\int_t^0[\gamma_s+\Gamma_\Omega(s)+i\delta_s]\mathrm{d}s}$ with Γ_Ω and Q defined in Eqs. (7)–(8). Since the efficiency has the form of an inner product between the function h_Ω and $\mathcal{E}^*_{in}(t)$, the maximal overlap appears for $h_\Omega(t) \propto \mathcal{E}^*_{in}(t)$ [16]. When both $\mathcal{E}_{in}(t)$ [Eq. (C10)] and Ω are real functions and $\Delta = 0$, we obtain the condition

$$\mathrm{Im}(h_\Omega(t)) = 0, \tag{E2}$$

which is satisfied at all time for $\delta_s = 0$. Note that, in principle, nonzero δ_s can counter nonzero Δ by setting at all times $\mathrm{Im}(\Gamma_\Omega) + \delta_s = 0$, because then $\Gamma_\Omega + i\delta_s = \gamma_\Omega + i[\mathrm{Im}(\Gamma_\Omega) + \delta_s] = \gamma_\Omega$ is real. However, since $\gamma_\Omega \leqslant |\Gamma_\Omega|$ (with equality if-and-only-if $\Delta = 0$), one has to increase Ω to compensate for this reduction. It is therefore always preferable to set $\Delta = 0$, maximizing the dynamic range of γ_Ω. This is especially important if $|\Omega(t)| \leqslant \Omega_{max}$ is bounded (due to experimental constraints, for example).

In the second stage of the storage ($\mathcal{S} \to \mathcal{K}$), the exchange evolution depends on the exchange rate $\tilde{J}(\delta) = \sqrt{J^2 + (\delta + i\gamma_s)^2/4}$, which in turn depends only on $\delta = \delta_k - \delta_s$ [14] and is optimal for $\delta = 0$. Therefore, fixing $\delta_s = \delta_k = 0$ attains that optimum. We therefore conclude that the choice of $\delta_s = 0$ maximizes the efficiency of sequential storage. In the adiabatic scheme, after adiabatic elimination of the electron spin coherence in the low-bandwidth limit, the nuclear spin coherence is given by [14]

$$\mathcal{K}(0) = \int_{-\infty}^{0} h_J(t)\mathcal{E}_{in}(t)\mathrm{d}t, \tag{E3}$$

with $h_J(t) = \xi a_J e^{-\int_t^0[\gamma_k+\xi\Gamma_J(s)+i\delta_k]\mathrm{d}s}$, where $\Gamma_J = J^2/[\Gamma_\Omega + \gamma_s + i\delta_s]$ and $a_J = iQ\Omega^*\Gamma_J/J$. Maximal storage efficiency is obtained when this integral is maximized. Considering this integral as an inner product, the maximum is now attained for $h_J(t) \propto \mathcal{E}^*_{in}(t)$. For real $\mathcal{E}_{in}(t)$, Ω and for $\Delta = 0$, the condition is now

$$\mathrm{Im}(h_J(t)) = 0. \tag{E4}$$

Here, δ_s takes the role of Δ in a standard Λ-system storage [16]. However, in contrast to a standard Λ-system, J is a constant making $\mathrm{Re}(\Gamma_J) \leqslant \frac{J^2}{\gamma_\Omega+\gamma_s}$ bounded. To exploit its full range, one must set $\delta_s = 0$, saturating the inequality. Consequently Γ_J is real (and a_J has a constant phase), making the choice $\delta_k = 0$ optimal. The results in this Appendix are consistent with our numerical results.

APPENDIX F: INTERMEDIATE SOLUTIONS IN SPIN-EXCHANGE-BASED MEMORIES

It is also interesting to consider the numerical solution when crossing from the ultralow bandwidth to high bandwidth, when the optimal solutions change from the adiabatic regime to the sequential regime, respectively. In this Appendix, we specifically focus on spin-exchange-based memories in the strong-coupling regime ($J \gg \gamma_s$) because they can maintain high storage efficiency for such variable bandwidth. In Fig. 6, we show the temporal shape of the electronic $\langle \hat{\mathcal{S}}^\dagger \hat{\mathcal{S}} \rangle$ and nuclear $\langle \hat{\mathcal{K}}^\dagger \mathcal{K} \rangle$ collective spin excitations for the different pulse bandwidths B corresponding to the symbols in Fig. 3(d). The leftmost plot shows a purely adiabatic solution where the low-bandwidth input field is slowly stored directly onto the noble-gas spins. Conversely, the rightmost plot shows the dynamics in the sequential regime, where the high-bandwidth input field is stored first on the alkali spin, and only later transferred onto the noble-gas spins via a resonant spin-exchange process. These two solutions were already shown in Figs. 3(e)–3(f). The two middle plots, on the other hand, show intermediate, mixed solutions that are neither purely adiabatic nor purely sequential. In this intermediate regime, the input field is stored first on a state that has both $\hat{\mathcal{S}}$ and $\hat{\mathcal{K}}$ characters. Later on, this state is rotated fully into $\hat{\mathcal{K}}$ via the spin-exchange coupling. Our numerical optimization shows, therefore, that efficient solutions can be engineered for intermediate bandwidth.

[1] A. I. Lvovsky, B. C. Sanders, and W. Tittel, Optical quantum memory, Nat. Photon. **3**, 706 (2009).

[2] J. L. O'Brien, Optical quantum computing, Science **318**, 1567 (2007).

[3] K. Heshami, D. G. England, P. C. Humphreys, P. J. Bustard, V. M. Acosta, J. Nunn, and B. J. Sussman, Quantum memories: Emerging applications and recent advances, J. Mod. Opt. **63**, 2005 (2016).

[4] N. Sangouard, C. Simon, H. De Riedmatten, and N. Gisin, Quantum repeaters based on atomic ensembles and linear optics, Rev. Mod. Phys. **83**, 33 (2011).

[5] K. Hammerer, A. S. Sørensen, and E. S. Polzik, Quantum interface between light and atomic ensembles, Rev. Mod. Phys. **82**, 1041 (2010).

[6] C. Gemmel, W. Heil, S. Karpuk, K. Lenz, C. Ludwig, Y. Sobolev, K. Tullney, M. Burghoff, W. Kilian, S. Knappe-Grüneberg, *et al.*, Ultra-sensitive magnetometry based on free precession of nuclear spins, Eur. Phys. J. D **57**, 303 (2010).

[7] T. R. Gentile, P. Nacher, B. Saam, and T. Walker, Optically polarized ^{3}He, Rev. Mod. Phys. **89**, 045004 (2017).

[8] O. Katz, R. Shaham, E. S. Polzik, and O. Firstenberg, Long-lived entanglement generation of nuclear spins using coherent light, Phys. Rev. Lett. **124**, 043602 (2020).

[9] G. Reinaudi, A. Sinatra, A. Dantan, and M. Pinard, Squeezing and entangling nuclear spins in helium 3, J. Mod. Opt. **54**, 675 (2007).

[10] A. Serafin, M. Fadel, P. Treutlein, and A. Sinatra, Nuclear spin squeezing in helium-3 by continuous quantum nondemolition measurement, Phys. Rev. Lett. **127**, 013601 (2021).

[11] A. Dantan, G. Reinaudi, A. Sinatra, F. Laloë, E. Giacobino, and M. Pinard, Long-lived quantum memory with nuclear atomic spins, Phys. Rev. Lett. **95**, 123002 (2005).

[12] T. G. Walker and W. Happer, Spin-exchange optical pumping of noble-gas nuclei, Rev. Mod. Phys. **69**, 629 (1997).

[13] O. Katz, R. Shaham, and O. Firstenberg, Quantum interface for noble-gas spins based on spin-exchange collisions, PRX Quantum **3**, 010305 (2022).

[14] O. Katz, R. Shaham, E. Reches, A. V. Gorshkov, and O. Firstenberg, Optical quantum memory for noble-gas spins based on spin-exchange collisions, Phys. Rev. A **105**, 042606 (2022).

[15] A. V. Gorshkov, A. André, M. Fleischhauer, A. S. Sørensen, and M. D. Lukin, Universal approach to optimal photon storage in atomic media, Phys. Rev. Lett. **98**, 123601 (2007).

[16] A. V. Gorshkov, A. André, M. D. Lukin, and A. S. Sørensen, Photon storage in λ-type optically dense atomic media. I. Cavity model, Phys. Rev. A **76**, 033804 (2007).

[17] J. S. Kollath-Bönig, L. Dellantonio, L. Giannelli, T. Schmit, G. Morigi, and A. S. Sørensen, Fast storage of photons in cavity-assisted quantum memories, Phys. Rev. Appl. **22**, 044038 (2024).

[18] G. S. Vasilev, D. Ljunggren, and A. Kuhn, Single photons made-to-measure, New J. Phys. **12**, 063024 (2010).

[19] T. Utsugi, A. Goban, Y. Tokunaga, H. Goto, and T. Aoki, Gaussian-wave-packet model for single-photon generation based on cavity quantum electrodynamics under adiabatic and nonadiabatic conditions, Phys. Rev. A **106**, 023712 (2022).

[20] D. F. Phillips, A. Fleischhauer, A. Mair, R. L. Walsworth, and M. D. Lukin, Storage of light in atomic vapor, Phys. Rev. Lett. **86**, 783 (2001).

[21] M. Lukin, *Colloquium*: Trapping and manipulating photon states in atomic ensembles, Rev. Mod. Phys. **75**, 457 (2003).

[22] M. Hosseini, B. M. Sparkes, G. Campbell, P. K. Lam, and B. C. Buchler, High efficiency coherent optical memory with warm rubidium vapour, Nat. Commun. **2**, 174 (2011).

[23] B. Julsgaard, J. Sherson, J. I. Cirac, J. Fiurášek, and E. S. Polzik, Experimental demonstration of quantum memory for light, Nature (London) **432**, 482 (2004).

[24] K. Jensen, W. Wasilewski, H. Krauter, T. Fernholz, B. Nielsen, M. Owari, M. B. Plenio, A. Serafini, M. Wolf, and E. Polzik, Quantum memory for entangled continuous-variable states, Nat. Phys. **7**, 13 (2011).

[25] D. Saunders, J. Munns, T. Champion, C. Qiu, K. Kaczmarek, E. Poem, P. Ledingham, I. Walmsley, and J. Nunn, Cavity-enhanced room-temperature broadband Raman memory, Phys. Rev. Lett. **116**, 090501 (2016).

[26] O. Katz and O. Firstenberg, Light storage for one second in room-temperature alkali vapor, Nat. Commun. **9**, 2074 (2018).

[27] O. Lahad and O. Firstenberg, Induced cavities for photonic quantum gates, Phys. Rev. Lett. **119**, 113601 (2017).

[28] A. V. Gorshkov, A. André, M. D. Lukin, and A. S. Sørensen, Photon storage in λ-type optically dense atomic media. II. Free-space model, Phys. Rev. A **76**, 033805 (2007).

[29] M. O. Scully and M. S. Zubairy, *Quantum Optics* (Cambridge University Press, Cambridge, 1999).

[30] C. Gardiner and P. Zoller, *Quantum Noise: A Handbook of Markovian and Non-Markovian Quantum Stochastic Methods with Applications to Quantum Optics* (Springer, Berlin, Heidelberg, 2004).

[31] R. Shaham, O. Katz, and O. Firstenberg, Quantum dynamics of collective spin states in a thermal gas, Phys. Rev. A **102**, 012822 (2020).

[32] V. Lefevre-Seguin and M. Leduc, Metastability-exchange and depolarising collisions in xenon and krypton, J. Phys. B **10**, 2157 (1977).

[33] T. Xia, S. Morgan, Y.-Y. Jau, and W. Happer, Polarization and hyperfine transitions of metastable ^{129}Xe in discharge cells, Phys. Rev. A **81**, 033419 (2010).

[34] M. Batz, P.-J. Nacher, and G. Tastevin, Fundamentals of metastability exchange optical pumping in helium, in *Journal of Physics: Conference Series* (IOP Publishing, Munich-Ismaning, Germany, 2011), Vol. 294, p. 012002.

[35] J. Dupont-Roc, M. Leduc, and F. Laloë, New value for the metastability exchange cross section in helium, Phys. Rev. Lett. **27**, 467 (1971).

[36] L. D. Schearer, Collision-induced mixing in the 2^3p levels of helium, Phys. Rev. **160**, 76 (1967).

[37] D. Vrinceanu, S. Kotochigova, and H. R. Sadeghpour, Pressure broadening and shift of He($2^3P_{0,1,2}$)−He(2^3s) lines, Phys. Rev. A **69**, 022714 (2004).

[38] R. Shaham, O. Katz, and O. Firstenberg, Strong coupling of alkali-metal spins to noble-gas spins with an hour-long coherence time, Nat. Phys. **18**, 506 (2022).

[39] A. V. Gorshkov, T. Calarco, M. D. Lukin, and A. S. Sørensen, Photon storage in λ-type optically dense atomic media. IV. Optimal control using gradient ascent, Phys. Rev. A **77**, 043806 (2008).

[40] W. Heil, C. Gemmel, S. Karpuk, Y. Sobolev, K. Tullney, F. Allmendinger, U. Schmidt, M. Burghoff, W. Kilian, S. Knappe-

Grüneberg, *et al.*, Spin clocks: Probing fundamental symmetries in nature, Ann. Phys. **525**, 539 (2013).

[41] D. Budker and M. Romalis, Optical magnetometry, Nat. Phys. **3**, 227 (2007).

[42] N. B. Phillips, A. V. Gorshkov, and I. Novikova, Optimal light storage in atomic vapor, Phys. Rev. A **78**, 023801 (2008).

[43] N. B. Phillips, A. V. Gorshkov, and I. Novikova, Light storage in an optically thick atomic ensemble under conditions of electromagnetically induced transparency and four-wave mixing, Phys. Rev. A **83**, 063823 (2011).

[44] N. B. Phillips, A. V. Gorshkov, and I. Novikova, Slow light propagation and amplification via electromagnetically induced transparency and four-wave mixing in an optically dense atomic vapor, J. Mod. Opt. **56**, 1916 (2009).

[45] K. B. Dideriksen, R. Schmieg, M. Zugenmaier, and E. S. Polzik, Room-temperature single-photon source with near-millisecond built-in memory, Nat. Commun. **12**, 3699 (2021).

[46] M. Dąbrowski, R. Chrapkiewicz, and W. Wasilewski, Hamiltonian design in readout from room-temperature Raman atomic memory, Opt. Express **22**, 26076 (2014).

[47] K. Zhang, J. Guo, L. Chen, C. Yuan, Z. Ou, and W. Zhang, Suppression of the four-wave-mixing background noise in a quantum memory retrieval process by channel blocking, Phys. Rev. A **90**, 033823 (2014).

[48] N. Prajapati, G. Romanov, and I. Novikova, Suppression of four-wave mixing in hot rubidium vapor using ladder scheme Raman absorption, J. Opt. Soc. Am. B **34**, 1994 (2017).

[49] D. England, P. Bustard, J. Nunn, R. Lausten, and B. Sussman, From photons to phonons and back: A THz optical memory in diamond, Phys. Rev. Lett. **111**, 243601 (2013).

[50] S. Appelt, A. B.-A. Baranga, C. Erickson, M. Romalis, A. Young, and W. Happer, Theory of spin-exchange optical pumping of ^{3}He and ^{129}Xe, Phys. Rev. A **58**, 1412 (1998).

[51] J. Sherson, A. S. Sørensen, J. Fiurášek, K. Mølmer, and E. S. Polzik, Light qubit storage and retrieval using macroscopic atomic ensembles, Phys. Rev. A **74**, 011802 (2006).

[52] C. A. Muschik, K. Hammerer, E. S. Polzik, and J. I. Cirac, Efficient quantum memory and entanglement between light and an atomic ensemble using magnetic fields, Phys. Rev. A **73**, 062329 (2006).

[53] D. E. Rumelhart, G. E. Hinton, and R. J. Williams, Learning representations by back-propagating errors, Nature (London) **323**, 533 (1986).

[54] N. Qian, On the momentum term in gradient descent learning algorithms, Neural Netw. **12**, 145 (1999).